



UNIVERSITÀ
DEGLI STUDI
DI PADOVA



Bayesian Inference of the 1D Electron Density Profile within the WEST Tokamak using Interferometry

by

Daniel Jordan

A masters thesis presented to the University of Padova
in fulfillment of the thesis requirement for the degree of
Physics of Data

The research was carried out at Ghent University with onsite supervision from
Geert Verdoolaege - Associate Professor
Hao Wu - PhD Student

Remote supervision from the university of Padova was provided by
Lidia Piron - Assistant Professor

2023

Author's Declaration

I hereby declare that I am the sole author of this thesis. This is a true copy of the thesis, including any required final revisions, as accepted by my examiners.

I understand that my thesis may be made electronically available to the public.

Abstract

The electron density profile is a key parameter that affects the performance and stability of tokamak plasmas. To gain an understanding of turbulent particle transport many fusion devices are fitted with diagnostics capable of high-fidelity electron density profile measurements. For future fusion reactors such as DEMO, the design will be focused on fusion performance. This limits the diagnostics available whilst also pushing the plasma to the limits of its stability. It will be important to thoroughly make use of all available information for plasma control. Interferometry is a diagnostic that is planned to be implemented within DEMO and is currently implemented within the WEST tokamak. A Bayesian inference algorithm with a Gaussian process prior was developed to infer the electron density profile from WEST interferometry data. Both stationary and non-stationary kernels are trialled. Hyperparameters are handled with optimisation methods and a full Bayesian analysis; where the hyperparameters are marginalised. These methods are applied to synthetic interferometry data created from chosen ground truth electron density profiles and to interferometry data from a west shot where they can be compared to NICE [5]; an inference algorithm currently implemented on WEST data. The resulting inferences show that each technique can accurately infer specific ground truth profiles yet perform poorly on others. Further development is needed for a Bayesian inference method that performs well regardless of the ground truth profile.

Acknowledgements

A big thank you to Hao Wu, Jeffrey de Rycke, and Yangyang Zhang for their enlightening conversation and mentorship. I thank the rest of the team at infusion UGent, Geert Verdoolaege, Sven Van Loo, Jerome Alhage, Leonardo Caputo, and Joseph Hall for accepting me into their research group and including me in their research discussions. An extra thank you to Geert Verdoolaege for giving me this enriching opportunity.

Table of Contents

Author's Declaration	ii
Abstract	iii
Acknowledgements	iv
List of Figures	vii
1 Introduction	1
2 Background Theory of Bayesian Techniques and WEST Interferometry	6
2.1 The Tokamak	7
2.2 NICE	9
2.3 Bayesian Inference and the Simple Regression Problem	10
2.4 Interferometry and Polarimetry	20
2.5 Bayesian Inference for Interferometry	21
2.6 Chapter Summary	26
3 Experiment to Compare Various Implementations on Real and Synthetic Data	28
3.1 Methodology for hyperparameter MAP and full Bayesian experiment . . .	28
3.2 Resulting Desnity Profiles of each Implementation	34
3.3 Chapter Summary	40

4 Conclusion	41
References	43
APPENDICES	46
A Deriving the Closed Form Posterior Expressions	47
B Deriving the Marginal Likelihood and Loss Function Expression	50
C Complete Set of Distributions and Expressions for Reference	55
C.1 Gaussian Process Regression for Interferometry, Discluding Artificial Observations	55
C.2 Gaussian Process Regression for Interferometry, Including Artificial Observations	57
Glossary	60

List of Figures

1.1	The vacuum vessel that holds magnetically confined plasma within the WEST tokamak [1].	2
2.1	A tokamak and relevant magnetic fields that create the helical particle trajectory [10].	7
2.2	Magnetic flux surfaces [16].	9
2.3	Electron density profile inferred by NICE for an instance in time within the WEST tokamak.	11
2.4	Illustrating how many Gaussians can model a curved line and its uncertainty.	13
2.5	A visualisation of the simple regression problem and the various distributions involved in the Bayesian inference solution.	16
2.6	Polodial cross section showing the geometry of interfero-polarimetry lasers at WEST [7] and some example interferometry data.	20
2.7	An example mesh grid to aid visualisation of the triangular mesh grid interpolation used in the response matrix construction.	22
2.8	Hyperbolic tangent smooth step function for length scale, equation 2.26. Used to capture the drop at the edge of H-mode plasmas [3].	25
3.1	Common tokamak profiles used to generate synthetic interferometry data. .	29
3.2	An example distribution of n_e for $\rho = 0.54$ from the full Bayesian sampling method.	31
3.3	The distribution from which emcee proposal functions (moves) are selected based on performance in an Optuna evaluation.	32

3.4	A trace plot showing the amplitude samples left after a burn of 1000 and thin of degree 10 are applied to 6000 samples collected with the tuned moves. The integrated autocorrelation time and the effective sample size are shown as ‘iat’ and ‘ess’, respectively.	33
3.5	A typical set of magnetic flux surfaces and interferometry data from the WEST tokamak. The electron density profile; inferred by the NICE algorithm.	33
3.6	Electron density inference using the hyperparameter MAP method on synthetic interferometry data. The mean square error is shown as ‘mse’.	35
3.7	Electron density inference based on the full Bayesian method for synthetic interferometry data. The mean square error is shown as ‘mse’.	37
3.8	Electron density inference using the hyperparameter MAP method on real interferometry data from the WEST tokamak. The mean square error is shown as ‘mse’.	38
3.9	Electron density inference using the full Bayesian method on real interferometry data from the WEST tokamak. The mean square error is shown as ‘mse’.	39
3.10	Electron density inference on real data using the stationary kernel with manually adjusted parameters. The amplitudes are set to 100, with an experimental error of 0.03 and a length scale: 0.4, 0.6 and 0.75 from left to right. The mean square error is shown as ‘mse’.	40

Chapter 1

Introduction

Nuclear fusion, the process by which two light atomic nuclei combine to form a heavier nucleus, holds the promise of revolutionizing the world's energy landscape. With the ever-increasing demand for sustainable, clean, and virtually limitless energy sources, nuclear fusion has emerged as a leading candidate. Nuclear fusion, in contrast to the fission processes used in current nuclear power plants, presents a fundamentally safer and more sustainable option. The primary fuel for fusion, isotopes of hydrogen, is abundant and can be extracted from water sources. Fusion reactions produce no long-lived, highly radioactive waste, minimizing environmental hazards and long-term disposal issues. Recent advancements have reignited interest in the field, with notable breakthroughs such as the development of high-temperature superconducting magnets, which enable the efficient confinement of high-energy plasma. An excellent example is the rare earth barium copper oxide high-temperature superconducting magnets that are being deployed in the SPARC experimental reactor [4]. In February 2022, the UK-based JET laboratory reported that it had smashed its own world record for the amount of energy it could extract by squeezing together two forms of hydrogen, deuterium and tritium. The experiments produced 59 megajoules of energy over five seconds (11 megawatts of power), which was more than double what was achieved in similar tests back in 1997. Another breakthrough was announced in December 2022 by US scientists at the National Ignition Facility in California. They confirmed that they had achieved ignition for the first time, by firing up to 192 giant lasers into a peppercorn-sized fuel pellet and triggering a fusion reaction that released more energy than was put in by the lasers [17].

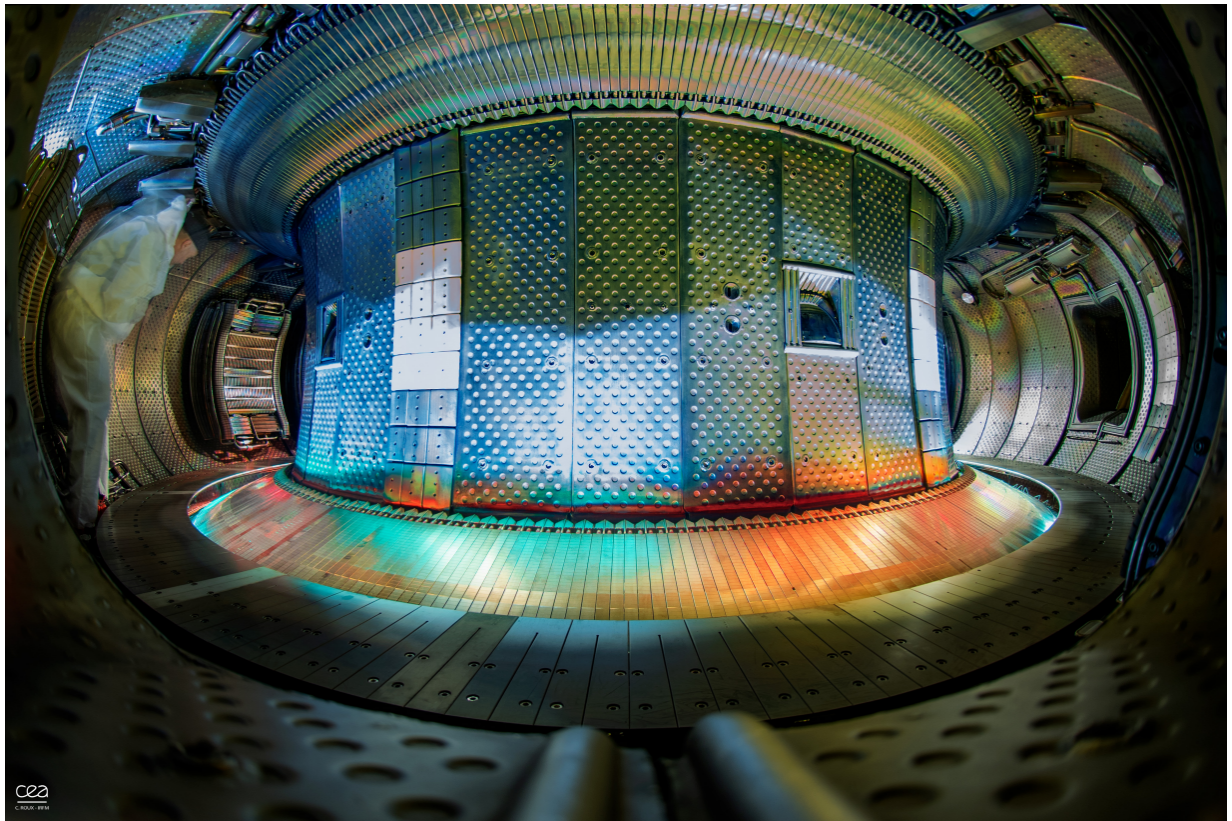


Figure 1.1: The vacuum vessel that holds magnetically confined plasma within the WEST tokamak [1].

Tokamaks are a class of fusion devices with great potential to achieve commercial fusion energy production. Tokamaks use magnetic fields to confine and heat plasma, a state of matter where atoms are split into electrons and nuclei. The immense pressures and temperatures created induce fusion reactions between light nuclei, such as hydrogen, to produce energy. Tokamaks currently demonstrate long plasma confinement times, which measure how well the plasma is isolated from the surrounding environment and affect the efficiency of energy production and heat loss. Tokamaks have the most extensive scientific and technological knowledge base, which has been accumulated over decades of research and development. This leads to reliable and robust designs, advanced diagnostics and control systems, and proven solutions for engineering challenges. These advantages make tokamaks the most promising candidates for achieving commercial fusion energy in the near future. Tokamaks have already shown impressive results in terms of fusion power output and energy gain. They are expected to reach even higher levels of performance with

the next generation of devices. Tokamaks are also supported by a strong international collaboration and a clear roadmap for development. Therefore, tokamaks have a huge potential to commercialise fusion before other methods: especially with ITER just around the corner and plans for DEMO already underway. ITER and DEMO are complementary projects that will advance fusion energy from the experimental stage to the commercial stage. ITER will provide the scientific and technological basis for DEMO, which will be the first fusion power plant to produce electricity and operate with a closed fuel cycle. The construction of ITER is expected to be completed by 2025, and the first plasma operation is planned for 2026. The full deuterium-tritium operation of ITER is scheduled for 2035, which will coincide with the start of the construction of DEMO. The operation of DEMO is foreseen to begin in the 2040s, and to demonstrate the viability of fusion energy for commercial use.

The electron density profile is a key parameter that affects the performance and stability of tokamak plasmas. It affects the plasma current, the confinement time, the energy transport, the magnetohydrodynamic (MHD) modes, and the coupling of external heating and current drive sources. There are physical limits that constrain the maximum achievable density in tokamak plasmas. One of the most well-known density limits is the Greenwald limit, which states that the line-averaged density cannot exceed a value proportional to the plasma current divided by the plasma cross-sectional area. This limit is empirically observed in many tokamaks, and attempts to exceed it result in disruptions or edge localized modes (ELMs). The physical mechanism behind the Greenwald limit is not fully understood, but it may be related to the stability of the edge pedestal, the bootstrap current, or the core particle transport. A lower electron density leads to runaway electrons. The electrons are accelerated around the tokamak by a central solenoid and only collisions prevent them from gaining enough energy to escape the magnetic confinement. A low density can mean that collisions are not frequent enough to prevent escape and the electrons can cause serious damage to the plasma facing wall. Thus it is not beneficial for the plasmas electron density profile to be such as to have many electrons with a low density near the edge.

One of the main challenges in measuring the electron density profile is to obtain high spatial and temporal resolution over a wide radial range. Several diagnostic techniques have been developed and applied to tokamaks, such as interferometry, reflectometry, Thomson scattering, and spectroscopy. Each technique has its own advantages and limitations in terms of accuracy, reliability, coverage, and invasiveness. A combination of different techniques is often used to obtain a comprehensive picture of the electron density profile evolution.

Another worthy challenge is to maintain the electron density profile in a desired shape.

The electron density profile is influenced by various factors, such as plasma geometry/magnetic configuration, plasma current and pressure, impurity content, fueling and pumping methods, and external heating and current drive sources. Some of these factors can be manipulated by the operators, others can be controlled in real time with sophisticated algorithms and feedback loops; achieving a favourable electron density profile that enhances the plasma performance and stability.

The electron density profile is an important parameter that determines many aspects of tokamak plasmas. Measuring and controlling the electron density profile is a crucial task for optimizing the tokamak operation and achieving fusion energy goals.

This thesis focuses on performing a Bayesian inference of the electron density profile using the interferometry diagnostic and a Gaussian process prior. Bayesian inference with a Gaussian process prior is a powerful technique for the nonparametric modelling of complex phenomena. A Gaussian process is a collection of random variables, which have a joint Gaussian distribution. A Gaussian process can be specified by a mean vector and a covariance matrix. By applying Bayes' rule, one can obtain the posterior distribution for an unknown profile, given some observed data. The posterior can be used for prediction and uncertainty quantification. Interferometry is a technique that uses the interference of electromagnetic waves to measure the properties of a medium. The interferometer within a tokamak consists of many laser beams penetrating the plasma at various angles. This thesis uses the **Tungsten (W) Environment in Steady-state Tokamak (WEST)** tokamak's laser geometry which covers a span of the poloidal cross section. Although there is not enough information to completely and accurately reconstruct the electron density profile a best guess given the data can be inferred. For real data, it is difficult or impossible to know how close any inferred profile is to the true profile.

Bayesian integrated analysis is often used to combine multiple diagnostics which measure the same or related physical parameters. This involves combining multiple diagnostics with the Bayesian framework which provides a universal way to treat uncertainties of any probability density function. R Fischer from the Max-Planck-Institut für Plasmaphysik published a paper on using Bayesian integrated analysis with Thomson scattering, interferometry and lithium beam diagnostics to combine their information on the electron density profile [6]. They focused on obtaining a systematic and formalized error analysis of all uncertainties involved in each diagnostic. These are then quantified within the likelihood. Jiahong Chen published a paper on the development of a Bayesian integrated analysis program developed for the HL-2A tokamak [2]. For the electron density profile, it combines interferometry and reflectometry. It aims to infer a 2D profile whilst this thesis focuses on a 1D profile. The program is a full Bayesian analysis from the raw data to the results. This thesis also aims to go from raw interferometry data to results in a fully

Bayesian way. GT von Nessi and MJ Hole also published a paper on the combination of interferometry and Thomson scattering to infer the electron density and temperature profile with Bayesian inference and Gaussian Processes [15]. Their work mainly focuses on the Thomson scattering diagnostic. Interferometry is not used to determine the shape of the profile but to contain the magnitude of the electron density given a profile shape. This avoids the difficult calibration of the integrated Thomson beam energy.

There is a common rhythm to these papers that is also echoed in my thesis. The problem is broken down with Bayes' theorem and the form of the various distributions are identified or defined. A forward model is defined that allows one to obtain an error free version of the data given a defined ground truth of the physical quantity of interest. The forward model is essential to computing the likelihood. The hyperparameters and their priors are identified and optimised using the hyperparameter **maximum a posteriori (MAP)** method or marginalisation. The posterior is computed with analytical expressions where possible or **Markov chain Monte Carlo (MCMC)** techniques are used to sample from the posterior. The posterior is presented as a probability distribution showing the most likely values of the physical quantity of interest and its uncertainty. There are many caveats and details that are specific to each implementation yet the overarching story remains intact. This thesis does not aim to combine multiple diagnostics but focuses on interferometry. The goal is to use raw interferometry data to infer the electron density profile with Bayesian techniques.

The background theory chapter introduces the tokamak and some necessary physics required to understand the assumptions made. The **WEST** tokamak has implemented **Newton direct and Inverse Computation for Equilibrium (NICE)** code to reconstruct the magnetic equilibrium and it also outputs the electron density profile as a byproduct. A brief description of **NICE**'s method is provided for comparison to the techniques in this thesis. Bayesian inference with Gaussian processes is introduced for a simple regression problem. It is introduced in such a way that the step to inferring the electron density profile from interferometry can be done simply by changing the forward model used. Some more advanced alterations to the process are explained to include further assumptions of the problem. Interferometry is explained in enough detail to understand how the density profile information is present within the data. The procedures explained in the background theory are then applied to synthetic interferometry data that was created with a ground truth profile assumption. This allows for a precise quantification of the performance through the mean square error. All of H mode, L mode and peaking are explored through synthetic data. Real interferometry data is taken from the **WEST** tokamak and the resulting inferred profiles can be compared to **NICE**.

Chapter 2

Background Theory of Bayesian Techniques and WEST Interferometry

This chapter aims to equip the reader with the necessary background theory required to reproduce this work and to understand the origin of the inferred electron density profiles presented in the results. It first describes a tokamak fusion device and some relevant physics concepts behind its function. It then describes in a high level manner the inference carried out by Blaise Faugeras and team with their code known as [NICE](#) [5]. After, the chapter outlines Bayesian inference and how a specific implementation can be used to solve a simple regression problem. Interferometry is introduced in enough detail to understand how the electron density profile could be inferred from its data. The Bayesian inference method introduced for the simple regression problem is then altered to allow this inference. Various options for advanced alterations are also explained here and explored in the results section.

2.1 The Tokamak

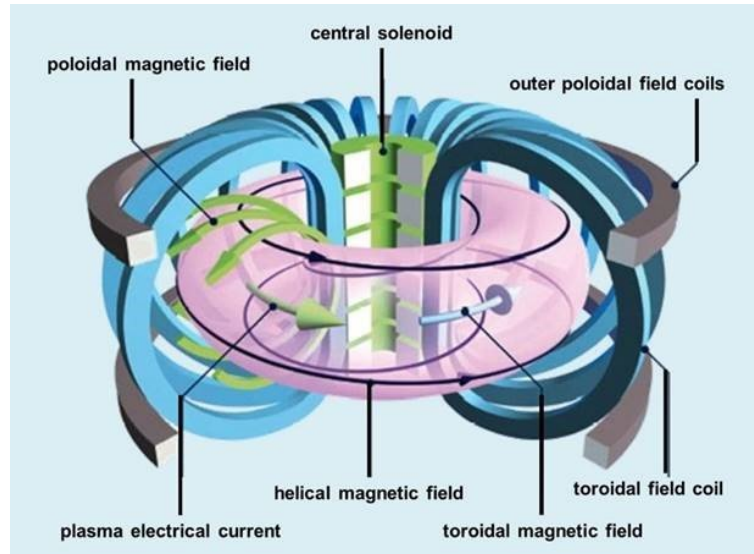


Figure 2.1: A tokamak and relevant magnetic fields that create the helical particle trajectory [10].

Tokamak is a class of fusion devices whose name comes from the abbreviation of a Russian phrase which means “toroidal chamber with magnetic coils”. It consists of a doughnut shaped vacuum chamber surrounded by powerful magnets that aim to confine a high temperature plasma that would otherwise damage the chamber. The plasma pressure and temperature are fundamental parameters in the context of nuclear fusion because they dictate the conditions required to overcome the electrostatic repulsion between positively charged atomic nuclei and bring them close enough for the strong nuclear force to initiate fusion reactions. In the core of stars like our Sun, the immense pressure and temperature generated by the gravitational collapse create the conditions where hydrogen nuclei (protons) can overcome their natural repulsion and fuse into helium, releasing a tremendous amount of energy in the process. To initiate fusion, hydrogen must be heated to temperatures in the range of 150 million Kelvin. In a tokamak, this is mainly accomplished with ohmic heating via a driving plasma current and neutral gas injection. This involves accelerating hydrogen ions to high speeds with electric fields and neutralising them the instant before they enter the chamber. The resulting plasma attains the required temperature, allowing nuclei to collide with sufficient energy for fusion reactions to occur. Figure 2.1 shows the position of various magnetic field coils within the tokamak. The toroidal

magnetic field exerts an inward force on the plasma thus raising its pressure. High pressure is required to increase the frequency of collisions so that the energy output can exceed the large heating energy input. The central solenoid induces a current in the plasma which produces the majority of the poloidal magnetic field. This field is essential for confinement but it also plays a key role in plasma stability. The outer poloidal field coils can be controlled in real time to help mitigate instabilities. A real time inference of the electron density profile would assist in identifying instabilities and informing the algorithm that drives the control coils to mitigate them. In addition to high temperature and pressure, the tokamak design seeks to maximize the confinement time of the plasma. This is essential to allow a sufficient number of fusion reactions to occur before the plasma cools down or loses its stability. The magnetic fields in a tokamak are carefully optimized to prevent rapid plasma loss and minimize heat loss through various mechanisms, including turbulent transport. The shape of the density profile has a large effect on the confinement time.

The combination of the toroidal and poloidal fields shown in figure 2.1 creates a helical magnetic field within the plasma. Electrons and ions are accelerated in opposite toroidal directions by the central solenoid yet both follow a trajectory along the magnetic field lines. This is because a charged particle moving across a magnetic field succumbs to a force perpendicular to its motion. This causes them to gyrate around the magnetic field lines and confines them to follow the magnetic field lines. This is an oversimplification and in reality there are drift phenomena that cause the particles to deviate from following the magnetic field lines exactly. Collisions also cause deviations. A detailed description of particle motion within a magnetic field is not needed for this thesis. It is enough to know that the particles in general follow the helical path of the magnetic field lines with a small gyration around the field line. In many models used for data analysis the assumption that particles follow the magnetic field lines is used, including within this thesis.

The magnetic field lines are confined to magnetic flux surfaces, figure 2.2. The toroidal and poloidal flux is constant on magnetic flux surfaces, there is 0 flux across magnetic flux surfaces. Since we assume that the particles follow the magnetic field lines which are strictly bound to these surfaces, we also assume that the density is constant on these surfaces. This allows the density of the entire cross-section to be expressed with a 1D profile as a function of normalised radius ρ for example, see NICE's profile, figure 2.3. The normalised radius is constant at each flux surface. It is 0 at the magnetic axis and 1 at the plasma boundary. The magnetic axis is the very center point of the core and is defined as where the poloidal magnetic flux is minimum and the plasma boundary is the last closed flux surface. Particles past the plasma boundary are no longer bound and may interact with the plasma wall. The existence of nested magnetic flux surfaces shown in figure 2.2 rely on the ideal magnetohydrodynamics (MHD) assumptions. Experiments frequently discover

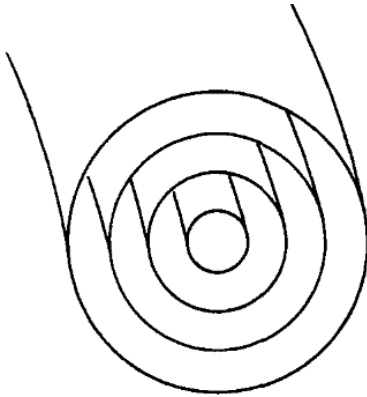


Figure 2.2: Magnetic flux surfaces [16].

magnetic islands which discredits the assumption of nested flux surfaces. The electron density profiles inferred by NICE and this work make the nested flux surface assumption, although for many applications such as real time control, a highly accurate inference is often not required.

2.2 NICE

NICE is an equilibrium reconstruction code that is routinely deployed for the WEST tokamak. It is relevant because it computes an inference of the electron density profile that is available for comparison to the profile inferred in this work, although NICE's main objective is to infer the shape and position of the magnetic flux surfaces. NICE uses magnetic diagnostics. At WEST these include 421 pickup coils, 36 flux loops and 12 Rogowski coils [12]. Magnetic diagnostics provide the majority of the information. NICE also uses interferometry, polarimetry, motional stark effect and pressure measurements. Equation 2.14 and 2.15 further in the chapter, show how interferometry and polarimetry together can provide information about the poloidal magnetic field, which directly affects the magnetic flux and thus magnetic flux surfaces. NICE performs the inference by minimising a cost function. The cost function determines how well a physical state of the system matches the data received. A state is a specific position and shape of the magnetic flux surfaces and electron density profile. This requires a forward model. The forward model takes a state of the system and attempts to compute the signals that would be received by error free diagnostics if that state was the ground truth. The forward model is a simplified mathematical representation of the measurement process and can never be 100% accurate. This introduces errors in the inference that need to be accounted for. The signals from

the forward model can be compared to the actual signals received by the diagnostics to compute the cost function. By minimising the cost function the state that best matches the data is found. [NICE](#) uses [Sequential Quadratic Programming \(SQP\)](#) as the minimisation algorithm. The optimal state of the system is then stored in the [Integrated Modeling and Analysis Suite \(IMAS\)](#) database for [WEST](#). This includes the 1D electron density profile used as a comparison for the profile inferred in this work. [NICE](#) also imposes regularisation terms on their cost function. These penalise the cost function when state properties have features that disagree with prior knowledge. This includes smoothness. We expect the magnetic flux surfaces and electron density profile, to be continuous and smooth. A state inputted into the cost function that is not smooth triggers the regularisation term which causes the cost function to be larger. Minimising the cost function now also leads to smooth magnetic flux surfaces and electron density profile. This leads to a difficult question, how smooth should it be? [NICE](#) also have a regularisation term to penalise the cost function if the electron density profile is far from 0 at the last closed flux surface or plasma boundary. It is prior knowledge that the electron density is near 0 at the plasma boundary. How close to 0, and how strong should the regularisation be is still an open question. This work's approach has direct analogues to these regularisation terms. As explained later in more detail the length scale controls smoothness and an artificial observation ensures the density is close to zero at the plasma boundary. Figure 2.3 shows an example of a [NICE](#) inferred electron density profile. It is modelled with a cubic spline function. It is the parameters of the cubic spline that are inputted into the cost function. The errors are calculated using a sensitivity method. In short, the error is deemed larger for the electron density of a particular normalised radius if a large change in the density leads to a small change in the cost function. In this case, we cannot be certain what density is better because many lead to a similarly low cost function and thus match the data similarly well. To include some more details, the [SQP](#) minimisation algorithm computes the hessian of the cost function for minimisation, but this hessian can also be used to measure the sensitivity and thus the errors. The diagonal of the hessian contains the second differential of the cost function for each input parameter. This describes the curvature of the cost function in the direction of each parameter. A smaller curvature means a smaller sensitivity and thus a larger error.

2.3 Bayesian Inference and the Simple Regression Problem

This work aims to use Bayesian inference to obtain the electron density profile. Bayesian inference will be introduced generally and then it will be used to define a specific imple-

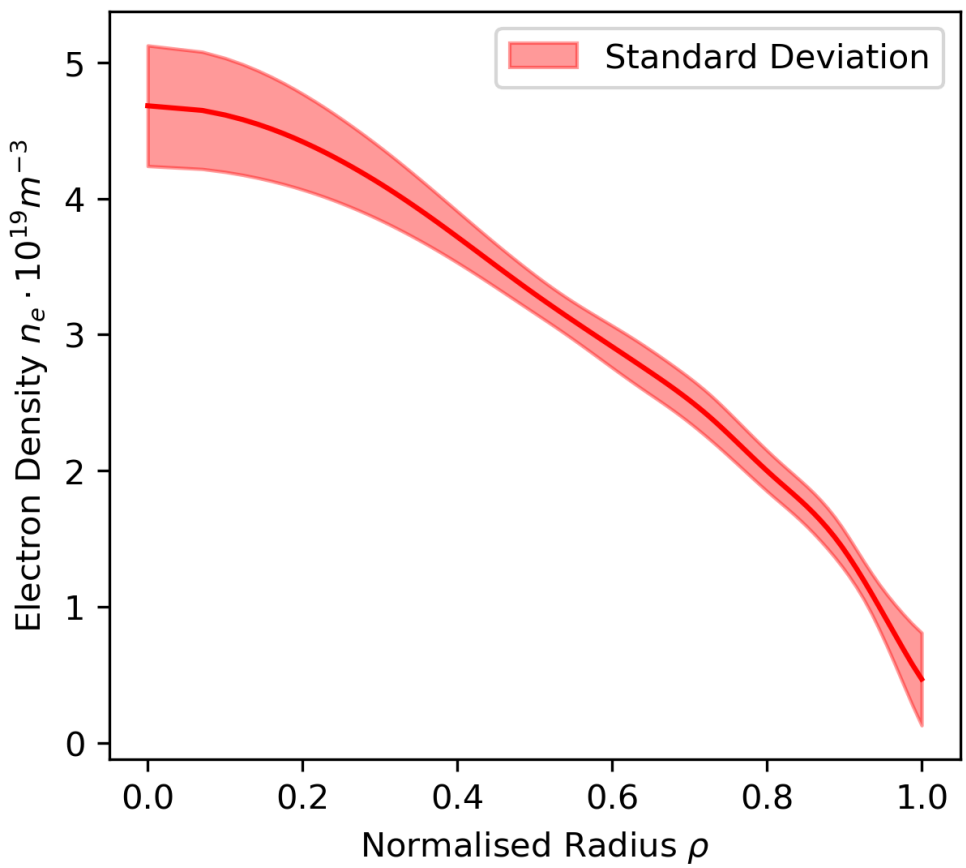


Figure 2.3: Electron density profile inferred by NICE for an instance in time within the WEST tokamak.

mentation applied to a simple regression problem. The method introduced will later be extended to solve the problem of inferring the electron density profile with interferometry data. The inferative Bayes' theorem for a physical quantity of interest q is expressed as,

$$P(q|D, I) = \frac{P(D|q, I)P(q|I)}{P(D|I)}, \quad (2.1)$$

the posterior $P(q|D, I)$ is the probability density distribution of q given the measured data D and some prior information I . The q that maximises the posterior is the most probable value of q given the data and prior information. The uncertainty of q can also be obtained from the posterior. The likelihood $P(D|q, I)$ is the probability density function that expresses the probability of the measured data given a fixed value of q and the prior information. The likelihood is described by the experimental error for the data collection. The prior $P(q|I)$ contains information assumed about q before the data is taken. The marginal likelihood or evidence $P(D|I)$ is simply the probability of the data given the prior information only. For posterior computation, the marginal likelihood serves as a normalisation factor. Normalisation is often carried out with other means to simplify the posterior computation. Although the marginal likelihood can be used to tune hyperparameters; as will be shown later.

The version of Bayes' theorem for a simple 1D regression problem is,

$$P(\vec{y}|\vec{d}, \vec{\epsilon}, \theta) = \frac{P(\vec{d}|\vec{y}, \vec{\epsilon})P(\vec{y}|\theta)}{P(\vec{d}|\vec{\epsilon}, \theta)}, \quad (2.2)$$

where \vec{y} contains the values of a curve at regular x values. The goal is to find the most likely \vec{y} given the data and prior information. \vec{d} contains curve measurements at known x values with some experimental errors $\vec{\epsilon}$. θ is a set of parameters related to the prior form, explained more later. The likelihood and prior are going to be clearly defined as multivariate Gaussians giving a multivariate Gaussian posterior which needs to somehow model the curve \vec{y} . Figure 2.4 illustrates how a multivariate Gaussian can model a curve. The functional form of a multivariate Gaussian is,

$$\mathcal{N}(\vec{y}, \vec{\mu}, \Sigma) = \frac{1}{\sqrt{(2\pi)^{\frac{n}{2}}|\Sigma|}} \exp \left[-\frac{1}{2}(\vec{y} - \vec{\mu})^T \Sigma^{-1} (\vec{y} - \vec{\mu}) \right], \quad (2.3)$$

the mean vector $\vec{\mu}$ holds the y values of the curve at regular intervals along the x axis. The diagonal of the covariance matrix holds the squared standard deviations of each Gaussian within the multivariate. These will be used to represent of the uncertainty of the curve

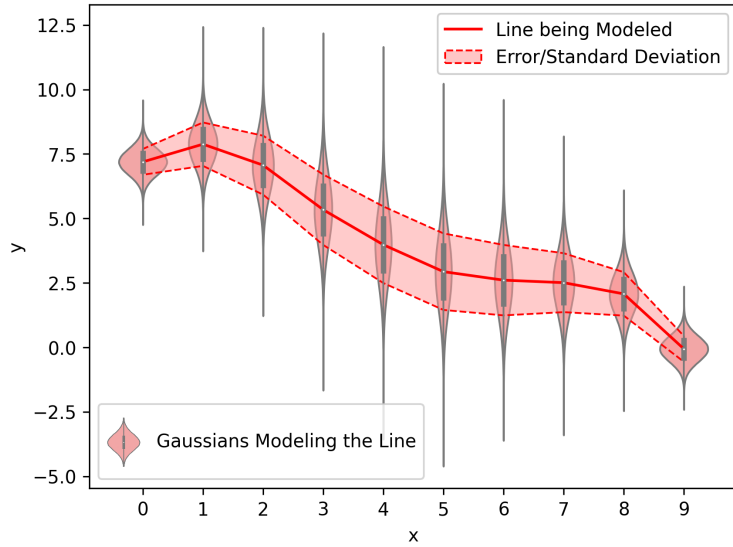


Figure 2.4: Illustrating how many Gaussians can model a curved line and its uncertainty.

inferred from the data. Figure 2.4 shows 10 Gaussians with each mean connected by a straight line. In practice, many Gaussians are used in a small space so that even a linear interpolation appears as a smooth curve. In our simple regression problem 101 Gaussians are used, thus \vec{y} has a length of 101.

For the simple 1D regression problem the posterior distribution is a multivariate Gaussian that represents the most likely curve given the data and prior information, see figure 2.5 for a visualisation. It can be expressed as,

$$\mathcal{N}(\vec{y}, \vec{\mu}_{post}, \Sigma_{post}), \quad (2.4)$$

where $/vec\mu_{post}$ has a length of 101, the same as the unknown y values. To compute μ_{post} and Σ_{post} we must define the likelihood and prior. If m measurements are taken the likelihood is defined as,

$$P(\vec{d}|\vec{y}, \vec{\epsilon}) = \mathcal{N}(\vec{d}, \vec{\mu}_{li} = R\vec{y}, \Sigma_{li}), \Sigma_{li} = \vec{\epsilon}I = \begin{bmatrix} \epsilon_1 & 0 & \dots & 0 \\ 0 & \epsilon_2 & \dots & 0 \\ \vdots & \vdots & \ddots & 0 \\ 0 & 0 & 0 & \epsilon_m \end{bmatrix}, \quad (2.5)$$

where R is the response matrix. Given some curve \vec{y} to be true, $R\vec{y}$ is a vector that has

the same length as \vec{d} and contains the values of the curve \vec{y} at the same x values that the data was collected at. The response matrix is an error free model of the measurement process. In the likelihood of figure 2.5 the blue line is an example of a given \vec{y} and if this was the ground truth and we took an error free measurement at the same x points as our original data then we would get the points indicated by the mean of each Gaussian. These points are computed with $R\vec{y}$ and provide the mean vector of the likelihood. The likelihood represents the probability of getting the black data points given the blue line \vec{y} is the ground truth. Regression is inherently an inverse problem and the response matrix is a forward model.

Here it is worth noting what a Gaussian process is and how a multivariate Gaussian is an approximation of it. A Gaussian process is a stochastic process that can be represented by a multivariate Gaussian of infinite dimensions. For example the x variable in 2.5 is continuous and thus has infinite values between 0 and 9. The curve that best fits the data is made of an infinite number of points, each point with an uncertainty. This can be modeled with an infinite number of Gaussians and thus the posterior can be said to be a Gaussian process. Since infinite precision is not possible with a computer a many dimension multivariate Gaussian is used, which is an approximation of the Gaussian process. Regression carried out with Bayesian inference and a Gaussian process prior is often referred to as Gaussian Process Regression; even when the finite dimension multivariate Gaussian approximation is used. The prior for this simple regression problem is a multivariate Gaussian. Although, the method being introduced is more general than the typical implementation of Gaussian Process Regression. This is so that it can easily be extended later to allow regression in situations where the data resides in a different space. To avoid confusion with the typical version of Gaussian Process Regression the term is not used for this implementation. For an introduction to typical Gaussian Process Regression, I suggest the textbook Gaussian Processes for Machine Learning [13]. The prior can be defined as,

$$\mathcal{N}(\vec{y}, \vec{\mu}_{pr} = \vec{0}, K), K_{ij} = k(x_i, x_j) = \sigma^2 \exp \left[\frac{(x_i - x_j)^2}{2l^2} \right], \quad (2.6)$$

where $\vec{0}$ is a vector of 101 zeros, the same length as \vec{y} . The zero vector is a commonly used ‘non-informative’ prior mean vector. The covariance matrix K is constructed using the kernel $k(x_i, x_j)$. The main role of the amplitude, σ , in the kernel is to set the prior strength. A high amplitude means the inference has a low prior strength and the resultant curve can be far from the prior mean $\mu_{pr} = \vec{0}$. See the prior in figure 2.5, the amplitude σ is the standard deviation of these Gaussians shown. For visualisation purposes only 5 prior Gaussians are shown in figure 2.5, yet in reality there are 101, the same number as there are unknown y values. The length scale, l sets the strength of the correlation between the

Gaussians. A low length scale means that only Gaussians close in x are highly correlated. Gaussians further in x would have a low correlation, meaning they can have a very different mean value. A low length scale allows the fitted curve to have more complexity similar to a high order polynomial and can lead to overfitting. A high length scale limits the fit's ability to curve sharply leading to a simple model, similar to a low order polynomial, leading to underfitting. A very high length scale leads to an almost linear fit. This prior is far from perfect. For instance, it is often known that the inferred values must be positive as you cannot have a negative electron density. Since the prior mean vector is set to $\vec{0}$, a negative value is as likely to be inferred as a positive value. Since it is Gaussian, values close to 0 are more likely to be inferred than values far from 0. To mitigate this a high amplitude can be used to lower the prior strength and allow the data in the likelihood to have more influence on the posterior result. The kernel $k(x_i, x_j)$ in equation 2.6 is known as the exponential square kernel. It is a very commonly used kernel but far from the only choice. The single value of the length scale prevents the inference from having long smooth regions with few features followed by regions of high variability. This can be an issue when inferring H-mode tokamak plasmas that have a sharp drop-off in density at the plasma edge. For these situations, a non-stationary kernel can be used that allows the length scale to be a function of x which can then allow for posteriors of varying complexity. Regardless of the kernel used, deciding the optimal values of its parameters for a problem is not obvious and various options will be explored.

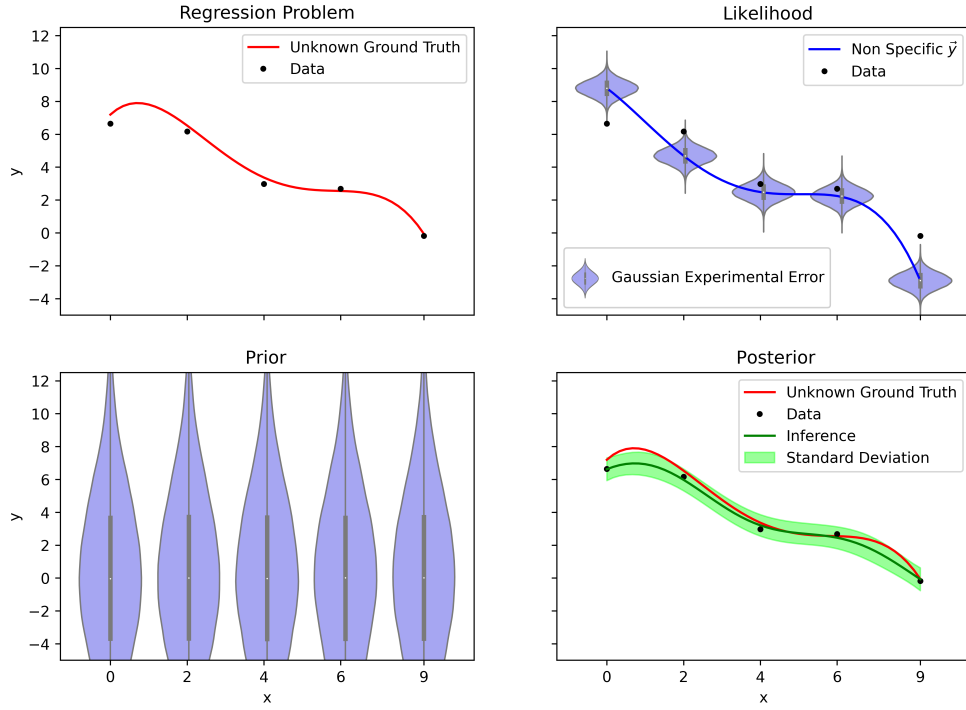


Figure 2.5: A visualisation of the simple regression problem and the various distributions involved in the Bayesian inference solution.

Figure 2.5 shows the simple regression problem, it then tries to show the Gaussians that make up the likelihood and prior although it is not perfect. We assume the observations are independent giving the likelihood a diagonal covariance matrix. So the multiple Gaussians that make up the likelihood are not dependent on each other, thus representing them individually provides all the information in the likelihood. The prior has a more complex covariance matrix K , and figure 2.5 does not have a complete representation of the priors form. Figure 2.5 also shows the 101 Gaussians that make up the posterior by plotting the regularly spaced $\vec{\mu}_{post}$ values in green with a green shadow showing the standard deviations of each Gaussian that are found in the diagonal of Σ_{post} . The posterior mean vector and covariance matrix can be computed with the closed form expressions,

$$\vec{\mu}_{post} = \vec{\mu}_{pr} + (K^{-1} + R^\top \Sigma_{li}^{-1} R)^{-1} R^\top \Sigma_{li}^{-1} (\vec{d} - R\vec{\mu}_{pr}), \quad (2.7)$$

$$\Sigma_{post} = (R^\top \Sigma_{li}^{-1} R + K^{-1})^{-1}, \quad (2.8)$$

which are derived in appendix A. The main steps include multiplying the functional forms of the prior and likelihood, ignoring all scaling factors, simplifying until they form a single unnormalised multivariate Gaussian and then comparing this with the posterior.

There is still the issue of deciding the values of the hyperparameters to place in K and the experimental error to place within Σ_{li} . Often the experimental error is not precisely known and can also be treated as a hyperparameter. To select the hyperparameters we can perform a separate hyperparameter Bayesian inference,

$$P(\theta, \vec{\epsilon} | \vec{d}) = \frac{P(\vec{d} | \theta, \vec{\epsilon}) P(\theta, \vec{\epsilon})}{P(\vec{d})}, \quad (2.9)$$

where the most probable hyperparameters given the same data can be found by maximising the hyperparameter posterior, $P(\theta, \vec{\epsilon} | \vec{d})$. This method is known as MAP. Notice the likelihood $P(\vec{d} | \theta, \vec{\epsilon})$ is exactly the marginal likelihood from the inferative Bayesian formula 2.1. The prior $P(\theta, \vec{\epsilon})$ needs to accurately represent our prior knowledge of the hyperparameters. By maximising the numerator of Bayes theorem the posterior is also maximised. The marginal likelihood from the hyperparameter Bayes theorem $P(\vec{d})$, can safely be ignored as it is a normalisation constant. All further mentions of marginal likelihood refer to the inferative distributions marginal likelihood $P(\vec{d} | \theta, \vec{\epsilon})$; as is the usual terminology for this procedure. It can be computed by integrating the numerator of the inferative Bayesian over the quantity of interest:

$$\begin{aligned} P(\vec{d} | \vec{\epsilon}, \theta) &= \int P(\vec{d} | \vec{y}, \vec{\epsilon}) P(\vec{y} | \theta) d\vec{y} \\ &= \frac{1}{(2\pi)^{\frac{m}{2}} \sqrt{|\Sigma_{li} + RKR^\top|}} \exp \left[-\frac{1}{2} (\vec{d} - R\vec{\mu}_{pr})^\top (\Sigma_{li} + RKR^\top)^{-1} (\vec{d} - R\vec{\mu}_{pr}) \right]. \end{aligned} \quad (2.10)$$

The values of the marginal likelihood can become very large and troublesome to compute with standard 64-bit float precision. For this reason, the logarithm is computed. It is the convention when performing optimisation to define a loss function to be minimised, thus the negative log marginal likelihood is used. Scaling constants do not affect the minimum value and can be ignored. The negative log marginal likelihood used as a loss function for hyper-parameters is then,

$$\text{loss}(\vec{\epsilon}, \theta) = \ln(|\Sigma_{li} + RKR^\top|) + (\vec{d} - R\vec{\mu}_{pr})^\top (\Sigma_{li} + RKR^\top)^{-1} (\vec{d} - R\vec{\mu}_{pr}), \quad (2.11)$$

the full derivation of this expression can be found in appendix B. To include a uniform prior for the hyperparameters $P(\theta, \vec{\epsilon})$, the loss function can be programmed to return infinity (or a very large number) when the proposed hyperparameters are outside their bounds. Although some minimisation algorithms can avoid proposing values outside of determined bounds.

An alternative solution is to perform a full Bayesian analysis where the hyperparameters are marginalised out of the inferative posterior. This allows the inferative posterior to become independent of the hyperparameters and allows for a more robust and flexible inference. Marginalisation of the posterior can be written as,

$$P(\vec{y}|\vec{d}) = \int \int P(\vec{y}, \theta, \vec{\epsilon}|\vec{d}) d\theta d\vec{\epsilon}, \quad (2.12)$$

and with conditional probability rules,

$$P(\vec{y}|\vec{d}) = \int \int P(\vec{y}|\theta, \vec{\epsilon}, \vec{d}) P(\theta, \vec{\epsilon}|\vec{d}) d\theta d\vec{\epsilon}. \quad (2.13)$$

Notice that $P(\vec{y}|\theta, \vec{\epsilon})$ is our original inferative posterior and $P(\theta, \vec{\epsilon}|\vec{d})$ is the hyperparameter posterior from earlier. Sampling \vec{y} from the joint distribution $P(\vec{y}|\theta, \vec{\epsilon})P(\theta, \vec{\epsilon}|\vec{d})$ is equivalent to sampling from the posterior $P(\vec{y}|\vec{d})$, that does not depend on the hyperparameters. To accomplish this a first step is to use MCMC sampling techniques to sample θ and $\vec{\epsilon}$ from the hyperparameter posterior. This only requires the ability to compute the log of the hyperparameter likelihood and prior given a proposed set of hyperparameters. The prior is defined by us and so must be computable and the likelihood is exactly the inferative marginal likelihood and has an analytical form given previously in equation 2.10. MCMC sampling involves initialising at a random position in the parameter space and using a stochastic proposal function to suggest a new position given the current position. If the new position satisfies the Metropolis Hastings criterion, it is accepted and the values of the hyperparameters at the new position are collected as a sample. Otherwise the sample is rejected and the proposal distribution suggests a new position. After some number of iterations, the samples closely represent samples from the true posterior. The first few samples are usually a poor representation of the posterior, especially if they are initialised far from the posterior maximum. For this reason, the first few samples are often discarded as a burn in. The final samples of θ and $\vec{\epsilon}$ can be used to sample \vec{y} from the inferative posterior $P(\vec{y}|\theta, \vec{\epsilon})$; which is a multivariate Gaussian of mean and covariance given by equations 2.7 and 2.8. Sampling from a known multivariate Gaussian can be done with more simple sampling techniques that have zero possibility of sample rejection:

[MCMC](#) sampling is not required. Remember that each sampled \vec{y} is a curve where the vector items correspond to y values of the curve at regularly spaced x intervals; as shown in figure 2.5. Thus the most likely value of the curve is the mean or median of the posterior samples at each x value. For uncertainty, the standard deviation of certain quantiles can be computed.

This thesis uses the Python package emcee for the [MCMC](#) sampling. This involves initialising a group of ‘walkers’ at random parameter positions. They then explore the space of the provided posterior distribution using a proposal function and the Metropolis-Hastings criteria. The proposal function suggests a new position in the hyperparameter space based on the current position.

An additional caveat of [MCMC](#) sampling is that the samples from a walker’s chain are autocorrelated, yet a true sample from the posterior would not depend on the current position of a walker. To reduce autocorrelation the chains are often thinned. Thinning by a degree of three means removing every third sample. This reduces autocorrelation and the samples more accurately represent samples from the posterior. Over-thinning limits the number of samples obtainable with the given computation power and time limits, leading to a loss of precision of the inference. To aid in deciding the thinning degree one can compute the [Integrated Autocorrelation Time \(IAT\)](#). This is a measure of how many steps it takes for a Markov chain to forget its initial state and become uncorrelated. Thinning by a degree of the [IAT](#) will ensure there is almost no autocorrelation between the samples but this is extreme and often means very long run times for a few samples that produce much less precise results than if more samples are kept.

Another way to reduce autocorrelation is to tune the [MCMC](#) algorithms hyperparameters. The proposal function often has tunable parameters. The choice of prior also plays a major role.

2.4 Interferometry and Polarimetry

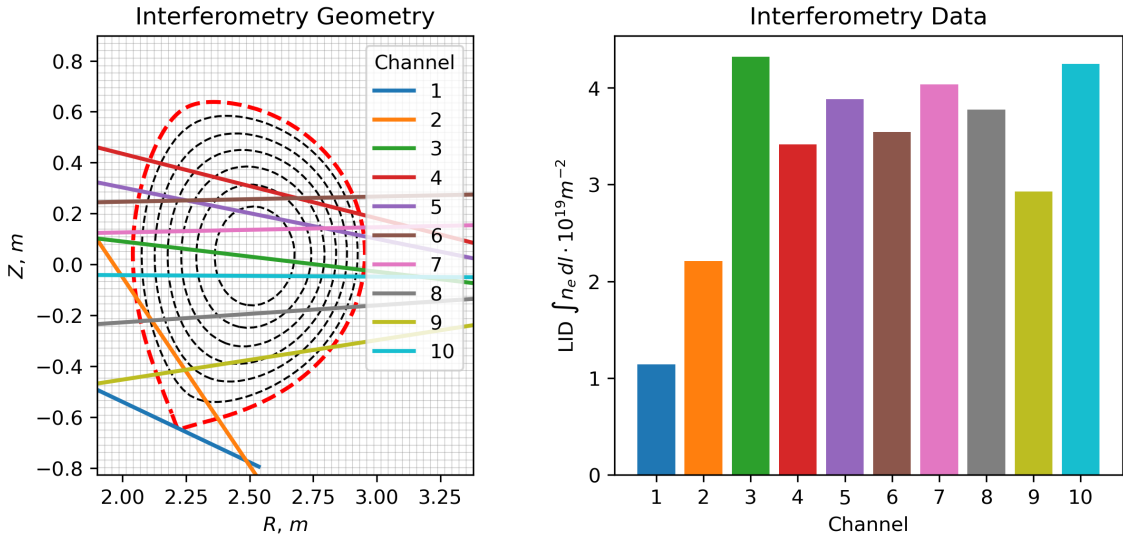


Figure 2.6: Poloidal cross section showing the geometry of interfero-polarimetry lasers at WEST [7] and some example interferometry data.

Interferometry and Polarimetry are techniques that use the interference of electromagnetic waves to measure the properties of a medium. Interfero-polarimetry lasers within a tokamak penetrate the plasma at various angles. The geometry at WEST is shown in figure 2.6. Each laser is split into two beams: one that passes through the plasma and one that bypasses it. The two beams are then recombined and detected by a receiver. The phase difference between the two beams depends on the difference in the optical path length, which is affected by the electron density along the line of sight. Interferometry measures the phase difference; allowing one to calculate the line integrated electron density of the plasma $\int n_e dl$,

$$\Delta\phi = \frac{\lambda e^2}{4\pi\epsilon_0 m_e c^2} \int n_e dl [9]. \quad (2.14)$$

The laser wavelength λ , is combined with other common physical constants to ascertain the constant of proportionality. WEST has stored the line integrated electron density as raw interferometry data in the IMAS database. This is the data that will be used for this

work. Although there is not enough information to completely and accurately reconstruct the electron density profile a best guess given the data can be inferred.

Polarimetry measures the Faraday rotation angle of the lasers. The linearly polarised lasers experience a rotation as the circularly polarised components travel through the plasma at different speeds. This is due to the small gyration of the electrons around the magnetic field. The Faraday rotation angle is proportional to the line integrated density of $n_e B_{\parallel}$ along the line of sight of the lasers,

$$\theta_F = \frac{\lambda^2 e^3}{8\pi^2 c^3 \epsilon_0 m_e^2} \int n_e B_{\parallel} dl [9], \quad (2.15)$$

where B_{\parallel} is the magnetic field strength parallel to the line of sight. Polarimetry has information about electron density and this work could be extended to become a Bayesian integrated analysis which includes this information in the inference. Only interferometry information is used in this thesis. Polarimetry can be used in combination with interferometry to gain information about the poloidal magnetic field and this is why **NICE** uses it to determine the position of the magnetic flux surfaces.

2.5 Bayesian Inference for Interferometry

To infer the electron density profile with interferometry, the previously defined regression process is altered. \vec{y} becomes \vec{n}_e , the $\vec{0}$ prior mean can remain the same. The amplitude σ and length-scale l can be re-optimised by maximising the marginal likelihood. The data is now in a different space and thus is the likelihood. The response matrix R must be created so that it will transform a profile \vec{n}_e into what would be measured by an error free version of the **WEST** interferometry system given \vec{n}_e is the true profile. The result of $R\vec{n}_e$ is a vector the same length as the data \vec{d} where each element corresponds to a different interferometry laser or channel.

The response matrix computation can be summarised in a few steps. **NICE** provides the magnetic flux at a set of grid points on the tokamak poloidal cross-section. It also provides the flux at a set of flux surfaces. The normalised radius ρ of each flux surface is known. A simple 1D interpolation can be used to determine the normalised radius at each grid point. Then using \vec{n}_e another 1D interpolation can be done to determine the electron density at each grid point. After the density at any point along a laser's line of sight $n_e(l_i)$, can be computed using triangular mesh interpolation. The density at the golden cross in figure 2.7 can be computed as a weighted sum of the density at the three nearest grid points $\{g_1, g_2, g_3\}$ that form the golden triangle,

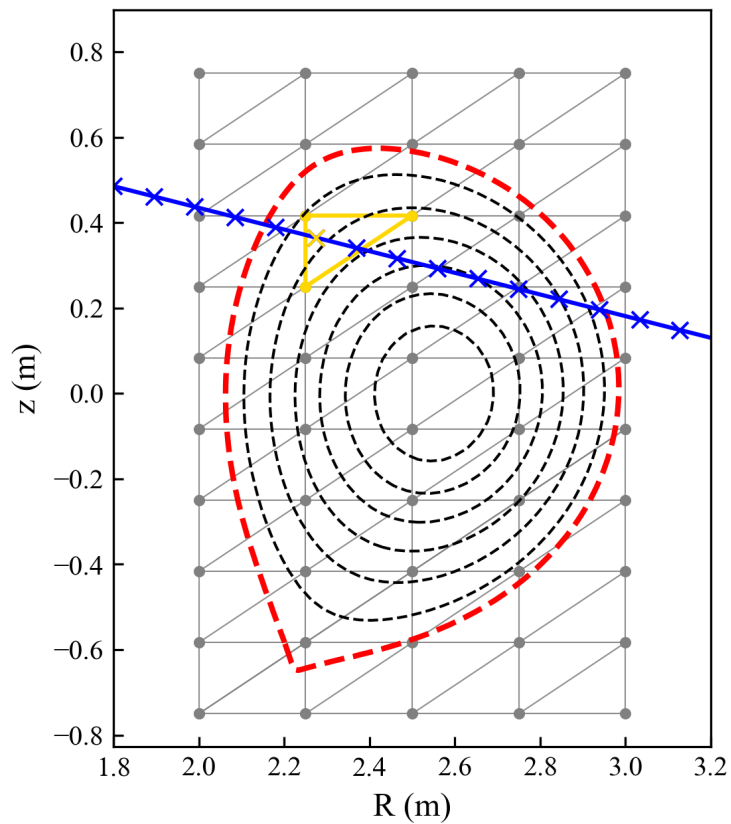


Figure 2.7: An example mesh grid to aid visualisation of the triangular mesh grid interpolation used in the response matrix construction.

$$n_e(l_i) = \lambda_1 n_e(g_1) + \lambda_2 n_e(g_2) + \lambda_3 n_e(g_3), \quad (2.16)$$

where λ values can be computed using the $(R_1, z_1), (R_2, z_2), (R_3, z_3)$ coordinates of the 3 known density points and the point of interest (R, z) ,

$$\lambda_1 = \frac{(z_2 - z_3)(R - R_3) + (R_3 - R_2)(z - z_3)}{(z_2 - z_3)(R_1 - R_3) + (R_3 - R_2)(z_1 - z_3)}, \quad (2.17)$$

$$\lambda_2 = \frac{(z_3 - z_1)(R - R_3) + (R_1 - R_3)(z - z_3)}{(z_2 - z_3)(R_1 - R_3) + (R_3 - R_2)(z_1 - z_3)}, \quad (2.18)$$

$$\lambda_3 = 1 - \lambda_1 - \lambda_2. \quad (2.19)$$

These λ values are known as the barycentric coordinates of the point of interest. The line integrated density can be approximated as a sum of electron densities at many points along the line of sight, l_i , times the width of their separation Δl ,

$$\int n_e dl \approx \sum_i n_e(l_i) \Delta l. \quad (2.20)$$

The contribution $w(g_i)$ of each grid point g_i is a sum of all the mesh interpolation coefficients λ_j used on that point,

$$\int n_e dl \approx \Delta l \sum_i w(g_i) n_e(g_i), \quad w(g_i) = \sum_j \lambda_j. \quad (2.21)$$

Each point can be associated with the nearest flux surface f_i equally spaced in ρ . This way the contribution $w(f_i)$ of each flux surface is a sum of the contribution at each of its associated grid points g_j ,

$$\int n_e dl \approx \Delta l \sum_i w(f_i) n_e(f_i), \quad f = \sum_j g_j. \quad (2.22)$$

All of these steps equate to a simple re-ordering of the original summation 2.20 to extract the contribution of each flux surface on the final integrated density value. Equation 2.22 can be computed using a vector product,

$$\int n_e dl \approx \Delta l \vec{w}^\top \vec{n}_e. \quad (2.23)$$

The contribution vector applies to one line of sight. The computation for all lines of sight can be performed by placing the $\Delta l \vec{w}$ vector for each line of sight as a row in the response matrix R . Thus, a vector of line integrated densities for the likelihood can be created,

$$\vec{\mu}_l = R \vec{n}_e. \quad (2.24)$$

This response matrix R can then be used in the closed form expressions 2.7 and 2.8, to perform a 1D electron density profile inference.

Some further alterations to the inference method can be made to further increase reliability. These include altering the kernel and adding artificial observations to include prior knowledge. The kernel can be changed to a non-stationary kernel,

$$K_{ij} = k(\rho_i, \rho_j) = \sigma^2 \left(\frac{2l(\rho_i)l(\rho_j)}{l(\rho_i)^2 + l(\rho_j)^2} \right)^{1/2} \exp \left(-\frac{(\rho_i - \rho_j)^2}{l(\rho_i)^2 + l(\rho_j)^2} \right), \quad (2.25)$$

this allows the length scale to change as a function of ρ . The length scale controls smoothness, model complexity and curvature. If these are free to change for different regions of the plasma then there is a greater range of possibilities for the final inference. A cubic spline function can be used for significant flexibility. This is where cubic functions are fitted to a set of points known as knots so that the second derivative of each cubic matches on each point. Chilenski used a hyperbolic tangent function,

$$l(\rho) = \frac{l_{core} + l_{edge}}{2} + \frac{l_{core} - l_{edge}}{2} \tanh \left(\frac{\rho - \rho_{step center}}{\rho_{step width}} \right) [3], \quad (2.26)$$

to form a smooth step down from a high length scale at the core to low at the edge, see figure 2.8. The extra freedom at the edge allows the inference to accommodate for a large sudden drop in electron density, which is a common feature for H-mode plasmas. H-mode plasmas are known to have a longer confinement time and thus better fusion performance. WEST does not operate in H-mode, although this method is tested with synthetic data from a simple H-mode simulation.

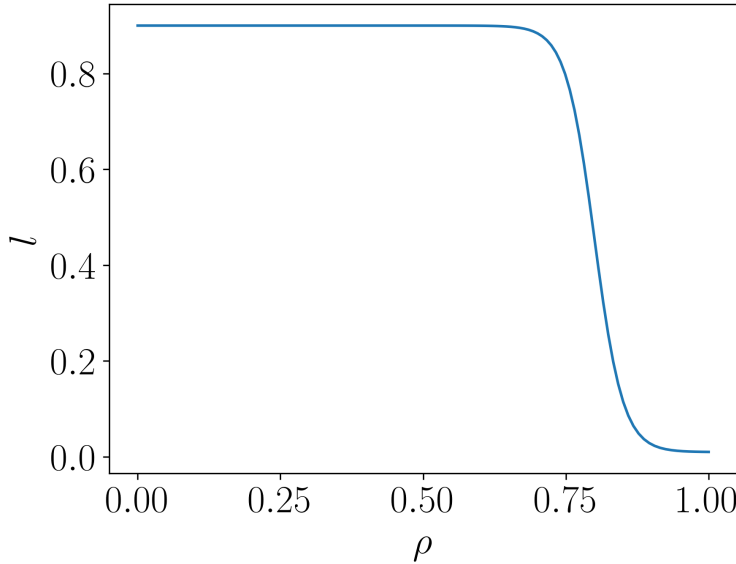


Figure 2.8: Hyperbolic tangent smooth step function for length scale, equation 2.26. Used to capture the drop at the edge of H-mode plasmas [3].

Traditionally prior information should be included in the prior distribution. However, in practice this often makes the required inversion of the priors covariance matrix difficult or impossible. This is either due to limited computational precision or because the covariance matrix becomes non-positive definite. The inversion is required because the closed form expressions for $\vec{\mu}_{post}$ and Σ_{post} involve inversions of both the likelihood and prior covariance matrices. Although the likelihood covariance matrix Σ_{li} is diagonal and so is certainly positive definite and inversion does not suffer from precision errors. This is not true for the priors covariance matrix K . It is difficult to define a prior covariance matrix that includes all the prior information, remains non-positive definite and does not suffer from precision errors. For these reasons, it is often more convenient to place prior information into the likelihood in the form of artificial observations. This method was also adopted by Chilenski [3]. The density is known to be close to 0 at the plasma boundary, ($\rho = 1$). It is also known that the density profile is smooth and symmetric meaning the gradient of the profile on the magnetic axis must be close to 0. This information can be included in the data, \vec{d} , with an artificial experimental error determining the strength of the information included in $\vec{\epsilon}$. Other parts of the method need to be altered to accommodate the new information. The vector to be inferred \vec{a} is not only \vec{n}_e but also includes $n_e(\rho = 1)$ and $n'_e(\rho = 0)$ concatenated onto the end. This allows the response matrix alteration to be simple,

$$R^{alt} = \begin{bmatrix} R_{m \times n} & O_{m \times 2} \\ O_{2 \times n} & I_{2 \times 2} \end{bmatrix} = \begin{bmatrix} R_{m \times n} & 0 & 0 \\ \vdots & \vdots & \vdots \\ 0 & \dots & 0 & 1 & 0 \\ 0 & \dots & 0 & 0 & 1 \end{bmatrix}, \quad (2.27)$$

where n is the number of unknown electron density values in \vec{n}_e and m is the number of interferometry lasers. The prior covariance matrix must also be altered. The covariance between a gradient and non-gradient data point is simply the differential of the covariance over the gradient data point. For two gradient data points, it is a differential over each point.

$$K'_{ij} = k'(\rho_i, \rho_j) = \frac{\partial k'(\rho'_i, \rho_j)}{\partial \rho'_i} [3], \quad (2.28)$$

$$K''_{ij} = k''(\rho'_i, \rho'_j) = \frac{\partial k''(\rho'_i, \rho'_j)}{\partial \rho'_i \partial \rho'_j} [3]. \quad (2.29)$$

In this notation ρ' indicates the position of a gradient data point. The alternate kernel is then,

$$K^{alt} = \begin{bmatrix} K & K' \\ K'^\top & K'' \end{bmatrix}. \quad (2.30)$$

The necessary adaptations to our defined Bayesian regression method to accommodate interferometry data have been described. For reference, the various final distributions and expressions after the adaptations are fully shown in appendix C.

2.6 Chapter Summary

The electron density profile is important as it plays a key role in determining the energy confinement time and informing real time control systems. With the assumption of magnetic flux surfaces, one can express it as a 1D profile. **NICE** is an equilibrium reconstruction code that also infers the electron density profile that can be used as a comparison in this thesis. Bayesian inference with multivariate Gaussians describing the various distributions can be applied to interferometry data to infer the electron density profile. A

non-stationary kernel can be used to allow the inference to have a model complexity that varies with ρ . Hyperparameters can be tuned by minimising the negative log marginal likelihood. Alternatively, the hyperparameters can be marginalised. Prior information can be easily included in the likelihood with artificial observations. In the results section, these methods will be deployed on synthetic data. The inference performance can be determined by how closely it fits the ground truth profile. They will also be deployed on real [WEST](#) data and the results will be compared to that obtained by [NICE](#).

Chapter 3

Experiment to Compare Various Implementations on Real and Synthetic Data

This chapter outlines the exact procedures that are carried out in an experiment to determine the performance capabilities of Bayesian inference for electron density profile inference within a tokamak.

The methodology goes through the values used for including prior information. It describes the algorithms used to compute the hyperparameter [MAP](#) and sample for the full Bayesian method.

The results systematically provide the inferences for each method on real and synthetic data. It includes an analysis of the findings.

3.1 Methodology for hyperparameter MAP and full Bayesian experiment

The previous section outlined the procedure for using Bayesian inference to solve a simple regression problem. It then expanded the concept to inferring the electron density profile with interferometry data. This included the possibility of placing prior information into the likelihood through artificial observations. The density at the plasma boundary is artificially observed to be 0 with an artificial Gaussian error of $0.5 \cdot 10^{19} m^{-3}$. The profile gradient at the magnetic axis ($\rho = 0$) is artificially observed to be 0 with a Gaussian error of 0.01.

[MAP](#) was introduced as a way to optimise the hyperparameters. The full Bayesian analysis method is introduced as marginalisation over the hyperparameters. The results from both methods will be presented. Both methods allow for hyperpriors to be included. A uniform prior is used for all hyperparameters and the bounds were selected by carefully observing how the parameters affect the resulting inference. The amplitude is constrained between 0 and 100 and is on the same scale as the electron density 10^{20} . Each length scale is bounded between 0 and 3 and is on the same scale as the normalised radius. This includes the two non stationary kernel options: hyperbolic tangent length scale and cubic spline length scale. 5 knots were used for the cubic spline. To reduce the dimensionality of the problem the knots were evenly spaced across the normalised radius. Each interferometry channel is given the same experimental error bounded between 0.03 and $0.3 \cdot 10^{19} m^{-2}$. [WEST](#) reports a no plasma noise in the order of $0.03 \cdot 10^{-19} m^{-2}$.

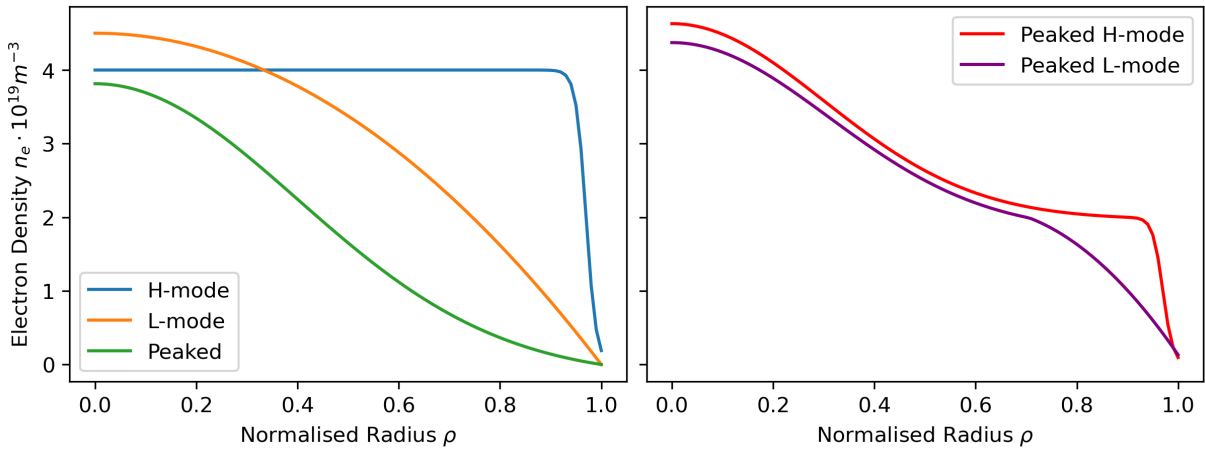


Figure 3.1: Common tokamak profiles used to generate synthetic interferometry data.

The mean squared error between the inferred profiles and synthetically created ground truth profiles will be computed. This allows precise performance comparisons between the kernels and hyperparameter methods. There are a few main profile types of interest to the scientific community. L mode or low confinement profiles are typically parabolic like in shape. They are the bread and butter of tokamak operations. It is the easiest profile to achieve and is often a stepping stone to achieving other profiles within a plasma shot. This is the main profile used within the [WEST](#) tokamak. H mode or high confinement mode is achieved by increasing external heating power from sources such as neutral beam injection and electron cyclotron resonance heating. H mode profiles have a distinct sharp drop in density near the plasma boundary. H mode profiles are well known for largely

increasing the energy confinement time of the plasma which is a crucial factor for net positive energy production; although H mode introduces extra instabilities known as ELMs. Another interesting profile feature is known as peaking. This is when the electron density in the core is increased, creating a peak or bell shaped profile. A peaked profile has been observed in many tokamaks and is due to turbulence and particle transport. The machine parameters that drive the peaking in the JET tokamak have been identified to be neutral beam injection heating [14]. Since high electron densities are needed in the core for a high fusion performance, peaked profiles need to be thoroughly understood. A peaked profile can be achieved with both L mode and H mode. The profiles are defined as shown in figure 3.1, and converted into synthetic error free interferometry data via the response matrix. The response matrix is created using real magnetic field lines inferred by NICE. A small Gaussian experimental error is added with a standard deviation of $3 \cdot 10^{17} m^{-2}$. This is what WEST reports as the no plasma noise of the interferometer.

The hyperparameter MAP is found by minimising the loss function based on the marginal likelihood, see equation 2.11. When any trialed parameters exceed their prior bounds the loss returns infinity (or a very high number). ‘SciPy minimize’ and ‘PyTorch SGD’ were both trialled and achieved similar results.

The full Bayesian approach involves using MCMC to sample from the hyperparameter posterior. This thesis uses the emcee python package which is based on the affine-invariant ensemble sampler proposed by Goodman and Weare [8]. This method uses many ‘walkers’ that explore the parameter space in parallel. They update their positions using the proposal function and the position of another walker. The advantage of this method is that it is invariant to affine transformations of the parameter space. Since a unique posterior distribution can be analytically computed from a single set of hyperparameters, sampling many sets of hyperparameters is equivalent to sampling many posterior distributions. Each posterior is a multivariate Gaussian that best fits the data given the sampled hyperparameters. This thesis uses the Scipy stats multivariate Gaussian random variable sampler, to sample one profile \vec{n}_e , from each posterior. Overall this is a way to sample \vec{n}_e from the joint distribution $P(\vec{n}_e|\theta)P(\theta|\vec{d})$, which is equivalent to sampling from the posterior $P(\vec{n}_e|\vec{d})$ that does not depend on the hyperparameters, θ . The mean density at each normalised radius forms the full Bayesian inferred profile. The standard deviation is computed for uncertainty. Using the mean and standard deviation allows for a direct comparison to the MAP results. The distribution of n_e at a point of the normalised radius is plotted to show it is Gaussian like, see figure 3.2. The median and quantiles are also acceptable measures.

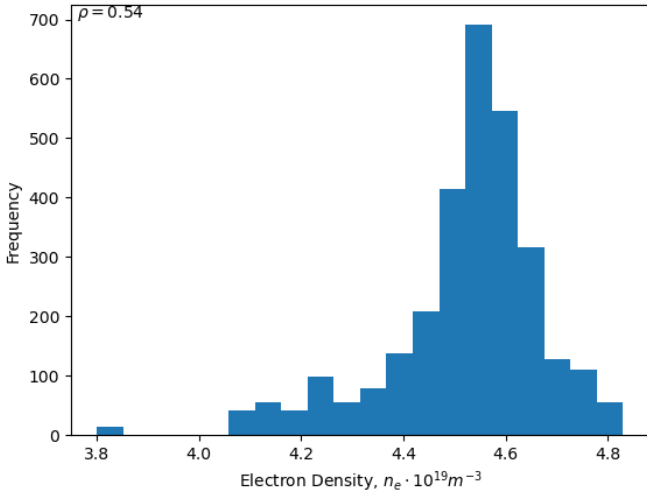


Figure 3.2: An example distribution of n_e for $\rho = 0.54$ from the full Bayesian sampling method.

To minimise autocorrelation the emcee hyperparameters are tuned. The main hyperparameter is called ‘moves’, which is their term for the proposal function. It is possible to pass multiple moves and weights when sampling. Emcee will randomly select a move in proportion to the weights. This should make the next sample more random and less correlated to the previous. Each move also has a single parameter. Optuna is a hyperparameter tuning framework for Python that proposes trials in an attempt to minimise the objective function. By default, it uses the tree-structured Parzen estimator algorithm. In this thesis four of the moves and their parameters are trialled with Optuna. Each trial was allowed to take 500 samples and 100 trials were made for the stationary kernel. The autocorrelation for each chain on each parameter is averaged. For each move, the trial with the lowest average autocorrelation time is found. The moves parameter value for this trial is recorded. The weights are calculated to allow the best performing move to be used more frequently, see figure 3.3.

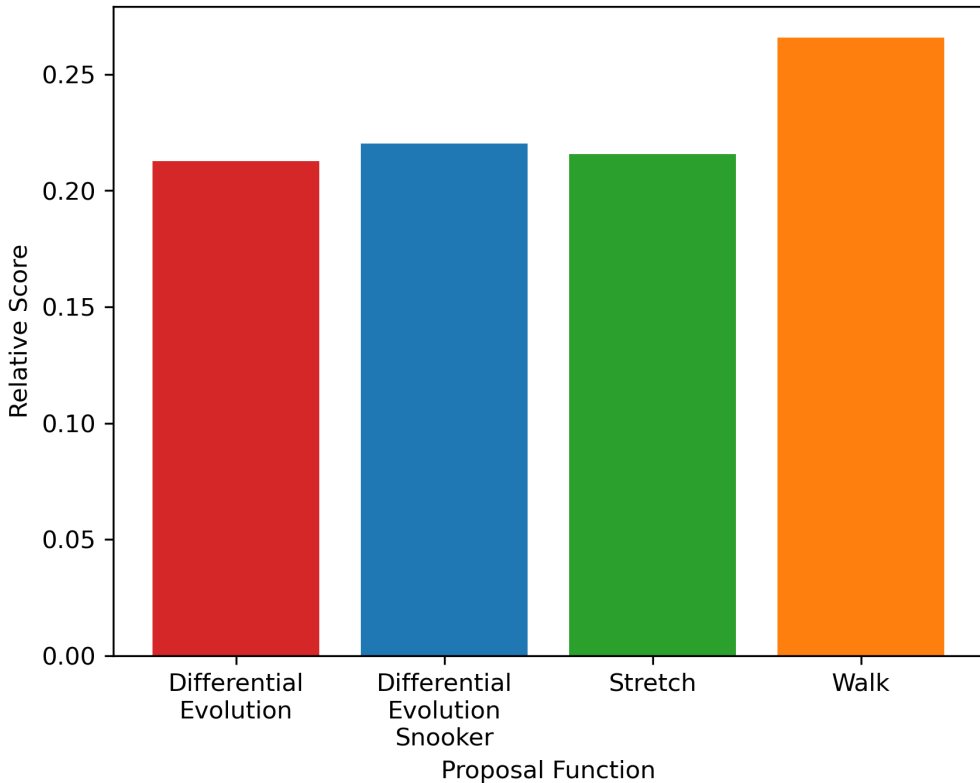


Figure 3.3: The distribution from which emcee proposal functions (moves) are selected based on performance in an Optuna evaluation.

Tuning the emcee moves was not repeated for each kernel to save on computation. For each full Bayesian inference 6000 samples are collected using the tuned moves, 1000 are burned and the rest are thinned by degree 10. An example chain of the remaining 500 samples has an integrated autocorrelation time of 23.6, see figure 3.4. This is still a significant amount of autocorrelation that could affect the reliability of the results.

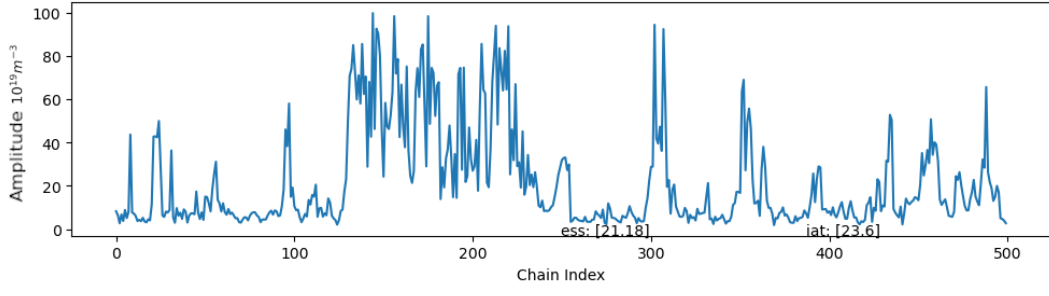


Figure 3.4: A trace plot showing the amplitude samples left after a burn of 1000 and thin of degree 10 are applied to 6000 samples collected with the tuned moves. The integrated autocorrelation time and the effective sample size are shown as ‘iat’ and ‘ess’, respectively.

The same analysis is executed for real interferometry data from the [WEST](#) tokamak. [WEST](#) operates in L mode and figure 3.5 shows a [NICE](#) inference for a typical set of interferometry data and magnetic flux surfaces.

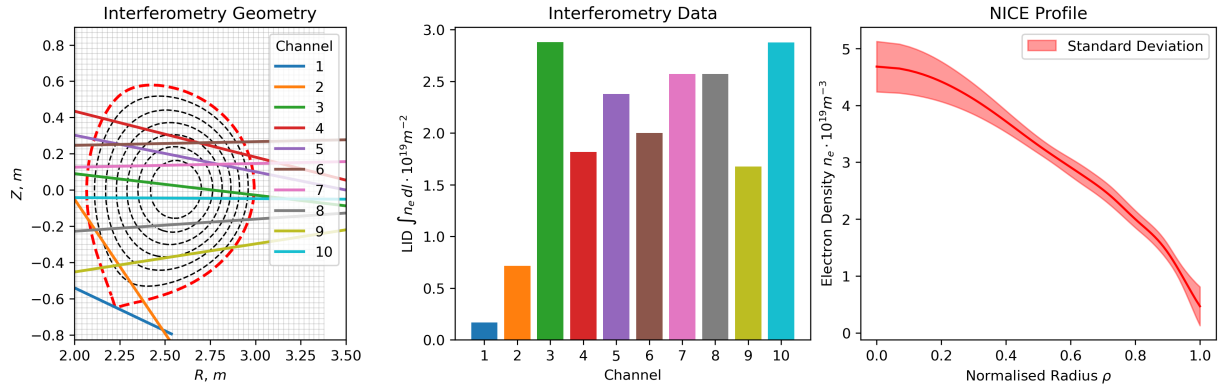


Figure 3.5: A typical set of magnetic flux surfaces and interferometry data from the [WEST](#) tokamak. The electron density profile; inferred by the [NICE](#) algorithm.

As seen in the results section there are some unexpectedly poor inferences. To determine if this is due to a limitation of the kernel, a manual adjustment of the stationary kernel is performed. This is in general not a true inference as it involves knowing a reference profile to approach.

3.2 Resulting Desnity Profiles of each Implementation

As expected the hyperbolic tangent was the most successful at inferring the H mode profile, see figure 3.6. This is because the constant flat top requires a high length scale yet the sharp drop requires a low length scale. A low length scale reduces the correlation between neighbouring inferred electron densities which is required for the high gradient at the edge. It is impressive how equally accurate and precise the three kernels are at inferring the L mode profile. The stationary kernel performed poorly when faced with a more complex shape such as the peaked L and H mode profiles. It appears close to parabolic and this is likely due to the inferred length scale being too large. The cubic spline length scale showcases its flexibility, allowing it to find some of the profile features although this appears to come at a price of smoothness. The hyperbolic tangent was able to find the H mode edge but not as closely as it was in the pure H mode profile. It still outperformed the other kernels for the H mode peak. The hyperbolic tangent has the lowest mean ‘mean square error’ over all the profiles at 0.053. Cubic splines are second with 0.076 and the stationary kernel performed the worst with 0.129, see figure 3.6.

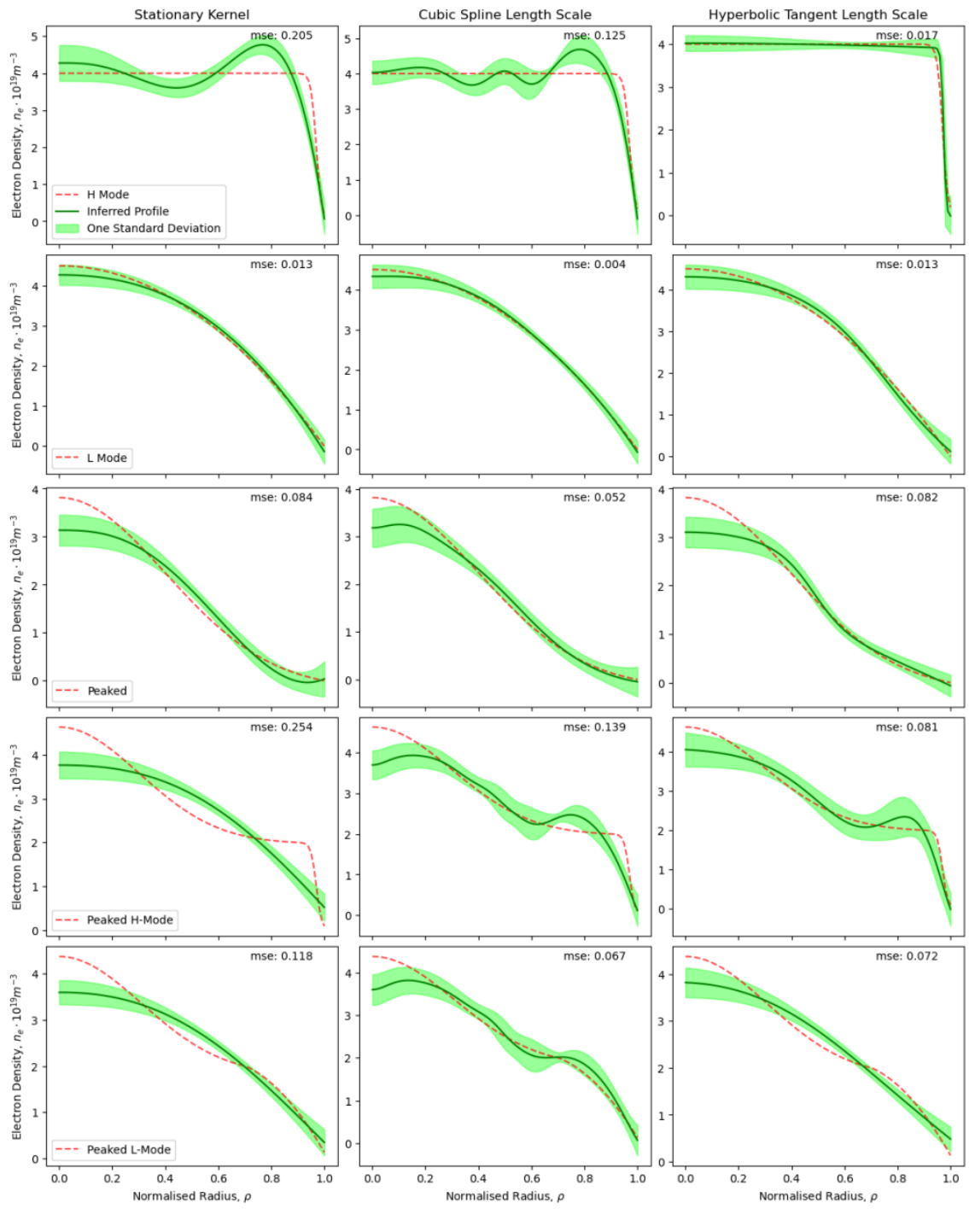


Figure 3.6: Electron density inference using the hyperparameter MAP method on synthetic interferometry data. The mean square error is shown as ‘mse’.

For the H and L mode profiles the full Bayesian analysis performed similarly well to the hyperparameter **MAP** method, see figure 3.7. The **MAP** method fits closer to the ground truth with an average mean squared error of 0.06 over the L and H mode profiles, compared to 0.13 for the full Bayesian method. Surprisingly the full Bayesian method performed poorly when faced with peaked profiles. It seems unable to follow the features of the profile and often conforms to a parabolic like shape. Both the **MAP** and full Bayesian methods have this issue with peaked profiles but the full Bayesian amplified the problems and caused it to occur for more of the profiles. Overall the inferences from the hyperparameter **MAP** method have an average mean squared error of 0.09 compared to 0.19 from the full Bayesian method.

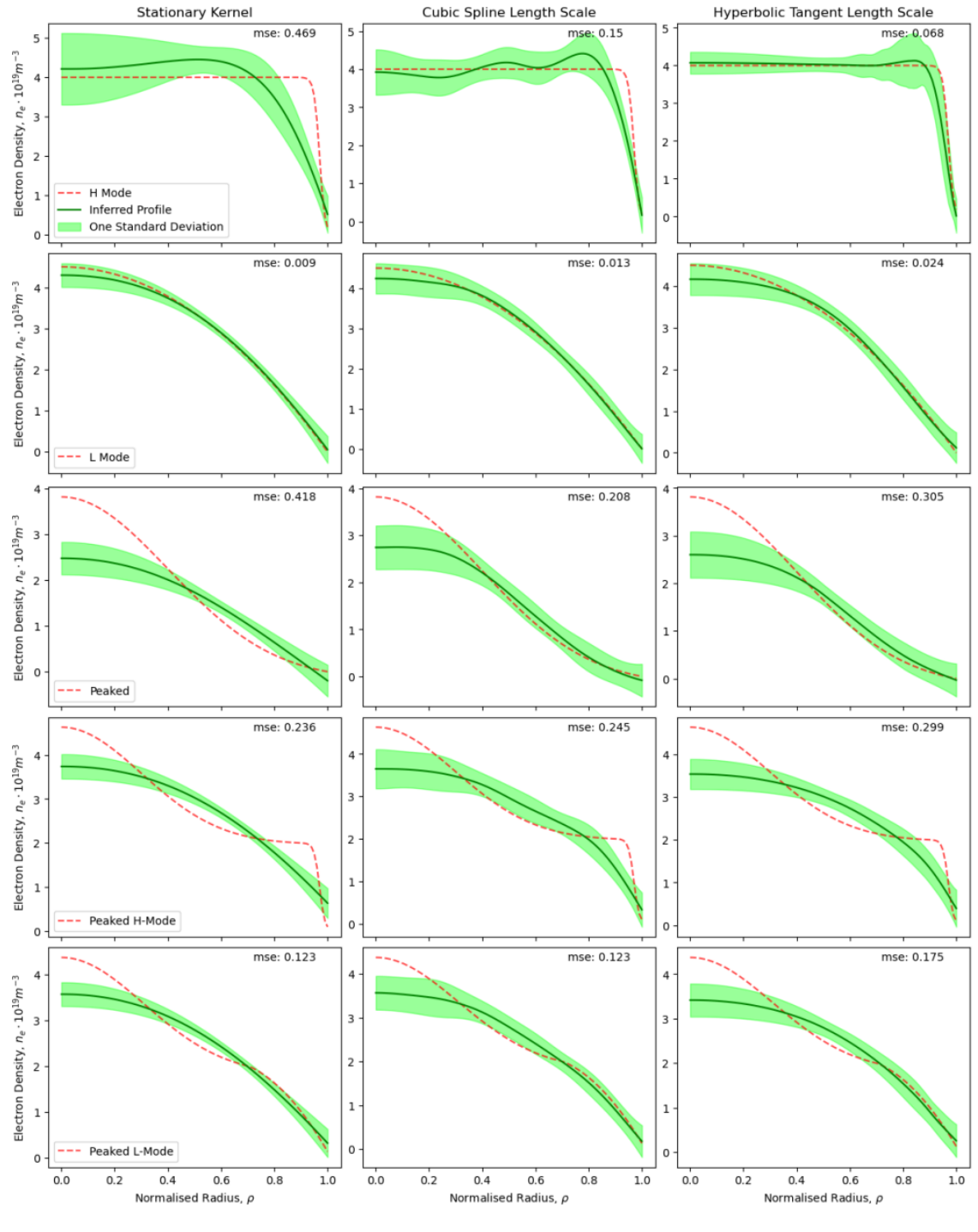


Figure 3.7: Electron density inference based on the full Bayesian method for synthetic interferometry data. The mean square error is shown as ‘mse’.

The same analysis is executed for real interferometry data from the [WEST](#) tokamak. The inferences from the hyperparameter MAP method are shown in figure 3.8. The L mode profile in [WEST](#) is often not close to a perfect parabola as used in the synthetic data investigation. As [NICE](#) has found, it often has an almost linear region in between the core and edge that flattens in the core and plunges to 0 near the edge. This happens with no attempts of peaking or high confinement. Despite being L mode, these extra features have caused the MAP method to struggle, see figure 3.8.

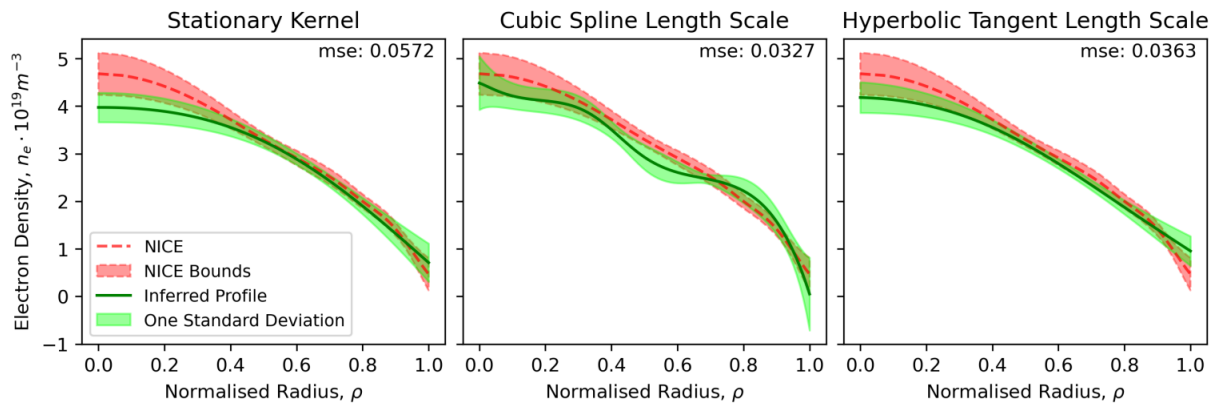


Figure 3.8: Electron density inference using the hyperparameter MAP method on real interferometry data from the [WEST](#) tokamak. The mean square error is shown as ‘mse’.

By comparing figures 3.8 and 3.9 we see that the mean square error shows that the MAP method is closer to [NICE](#) for both the cubic spline and hyperbolic tangent kernel. The stationary kernel performed similarly in both methods. However, the full Bayesian method with the hyperbolic tangent can find the small kink feature near the edge.

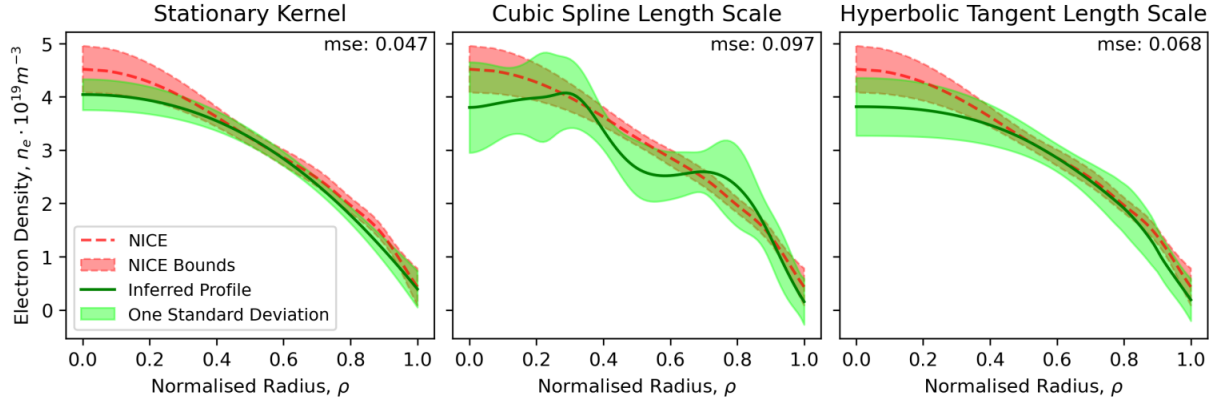


Figure 3.9: Electron density inference using the full Bayesian method on real interferometry data from the WEST tokamak. The mean square error is shown as ‘mse’.

The final method used to optimise the inference is manual intervention. For many of the inferences with the stationary kernel, the length scale seems to be too large as the inferred profile appears parabolic and fails to match the shape of the ground truth or NICE. Lowering the length scale manually allows the inference to have more freedom and match more features, see figure 3.10. This caused the mean ‘mean square error’ of the MAP method’s stationary kernel to drop from 0.15 to 0.03 for the three inferences manually adjusted. This indicates that the hyperparameter MAP method does not guarantee the most accurate possible inference. This manual intervention is in general not a true inference as it involves knowing a reference profile to approach. It was only performed to show that the kernels themselves are not at complete fault for poor results.

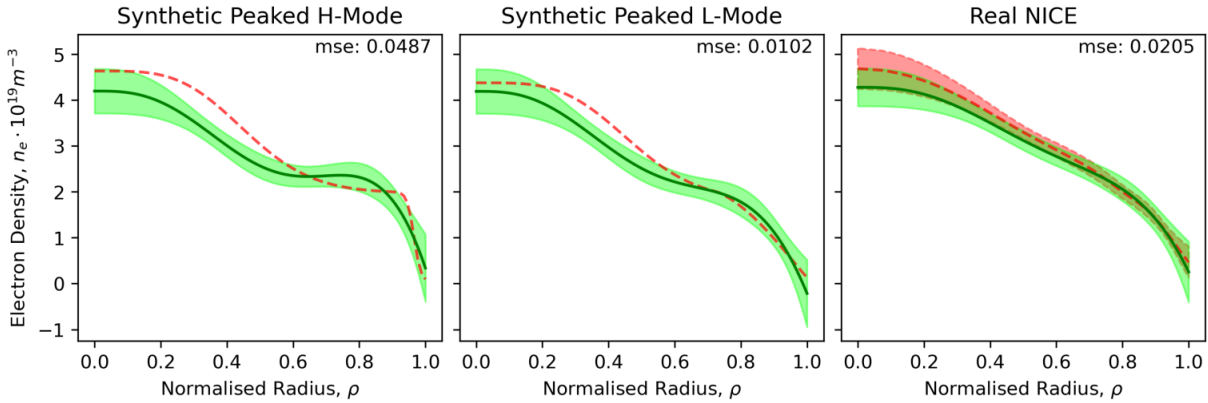


Figure 3.10: Electron density inference on real data using the stationary kernel with manually adjusted parameters. The amplitudes are set to 100, with an experimental error of 0.03 and a length scale: 0.4, 0.6 and 0.75 from left to right. The mean square error is shown as ‘mse’.

3.3 Chapter Summary

Each hyperparameter has been given a uniform prior with specific bounds. Artificial observations were included to ensure a density near 0 at the plasma boundary and a gradient near 0 at the magnetic axis. Five profiles of scientific interest have been created and used to generate synthetic interferometry data. Real data was collected for a typical shot from the [WEST](#) tokamak. An alternative inference from [NICE](#) is available for the real data. Optimisation techniques are used to determine the [MAP](#) of the hyperparameters. For the full Bayesian approach the proposal function of the [MCMC](#) sampler is tuned with Optuna. This was an attempt to reduce the autocorrelation. The autocorrelation remained unacceptably high and potentially undermines the credibility of the full Bayesian results. Profiles containing multiple features are difficult for any of the tested methods to approach. A strong H mode profile can be well inferred using a hyperbolic tangent kernel with both the [MAP](#) and full Bayesian approaches. A parabolic L mode profile can be well inferred with any of the kernels and approaches. The peaked profiles contain the most features and proved the most challenging to infer. From manually adjusting the stationary kernel a profile was found that more closely matches the peaked profiles and the NICE profile. This shows that the kernel is not the main component holding back the quality of the results. It is more likely that the true MAP has not been found and the autocorrelation is preventing the full Bayesian samples from representing the true posterior.

Chapter 4

Conclusion

The tokamak is the most researched device that has the highest chance of becoming a viable fusion reactor. Within the tokamak, it is vital to be able to measure the electron density throughout the device to ensure safety limits are maintained and fusion performance goals are met. The equilibrium of the tokamak plasma has toroidally symmetric flux surfaces on which the electron density is constant. The flux surfaces allow a 1D electron density profile to express the density throughout the tokamak. The flux surfaces are provided by the [NICE](#) code which uses magnetic diagnostic data to determine the flux surfaces. There are multiple diagnostics that can measure the electron density. This thesis focused on the interferometry diagnostic within the [WEST](#) tokamak. Interferometry is a technique that uses the optical path length difference of vacuum to plasma for multiple lasers fired through the plasma to determine the line integrated electron density along the laser's line of sight. This can provide enough information to infer the electron density profile with Bayesian techniques. Both real and synthetic data were used to test various Bayesian techniques. The various techniques were different ways to deal with the hyperparameters that defined the prior. Three different kernels were trialled that defined the functional form of the smoothness of the final inferred profile. The parameters in the kernels were decided using a [MAP](#) of the hyperparameter posterior or with a full Bayesian analysis which involves marginalising the hyperparameters by sampling from a joint probability distribution of the electron density profiles posterior and the hyperparameter posterior. Once the hyperparameters are known then the posterior of the density profile can be computed analytically; although this process requires matrix inversion. The prior information also included that we know the gradient is close to 0 in the core and the density is close to 0 at the last closed flux surface. This was included in the Bayesian analysis using artificial observations. [NICE](#) also provides an electron density profile for real [WEST](#) shots and can be compared to the Bayesian

methods.

Five synthetic profiles were defined and used to create synthetic interferometry data. These included L-mode, H-mode, Peaked, L-mode Peaked and H-mode Peaked. They are all scientifically relevant profile shapes. Real interferometry data from a typical [WEST](#) shot was also used. The inferred profiles of the synthetic data could be compared to the synthetic profiles and the inferred profiles from the real data could be compared to the [NICE](#) profile. The full Bayesian approach involves [MCMC](#) sampling which was carried out using the emcee python package. The emcee parameters are turned to minimise the autocorrelation. There was still substantial autocorrelation that reduced the reliability of the samples to be from the true hyperparameter posterior distribution. This reduces the credibility of this implementation of the full Bayesian approach. The final inferences show potential for the methods explored but are inconclusive as to which is the best method. There was no combination of the kernels and hyperparameter method that was able to perform well on all of the profiles of interest. A few of the inferences very well match the synthetic or [NICE](#) profile; although for a real scenario, there is no comparison profile to assess performance and the inference algorithm must be able to cope with any ground truth profile.

For future investigation, more optimisation techniques could be deployed for finding the [MAP](#) of the hyperparameter posterior of the various kernels. The cubic spline function for the hyperbolic tangent was the most flexible function used which should allow it to be the most effective for a wide variety of profiles, the number of spline knots and their prior positions could be better tuned to improve performance. The amplitude hyperparameter determines how far from the prior profile the inference can easily go. This is an intuitive parameter that could potentially be manually selected to reduce the dimensionality of the parameter space to be searched and increase the chance an optimal length-scale function could be selected. [WEST](#) also collects polarimetry data and this also contains information about the electron density profile. More work could be done to include this information in the Bayesian inference. This would involve using the temperature profile to get the current profile which could be used to get the poloidal magnetic field which could then separate the electron density from the poloidal magnetic field in the polarimetry phase shift shown in equation, [2.15](#). There is also information available about the amount of fuel injected into the system and this is correlated to the electron density. This could be used to get a more accurate prior for the electron density profile. Once the algorithm is stable and consistently provides accurate inferences then the next step would be to test the real-time capabilities. The slowest process is the hyperparameter optimisation and after that the matrix inversion. Perhaps these could be replaced with reduced models or neural networks to ensure real-time computation speeds.

References

- [1] CEA. Tokamak vacuum chamber, 2021. Accessed: 2023-11-17.
- [2] Jiahong Chen, Zhibin Wang, Tianbo Wang, Yonghao Yang, Hao Wu, Yonggao Li, Guoliang Xiao, Geert Verdooolaege, Didier Mazon, Zengchen Yang, Min Jiang, Zhongbing Shi, Jian Chen, Yi Yv, Wulyu Zhong, and Min Xu. Integrated data analysis on the electron density profile of hl-2a with the bayesian probability inference method. *Plasma physics and controlled fusion*, 65(5):55027–, 2023.
- [3] M.A. Chilenski, M. Greenwald, Y. Marzouk, N.T. Howard, A.E. White, J.E. Rice, and J.R. Walk. Improved profile fitting and quantification of uncertainty in experimental measurements of impurity transport coefficients using gaussian process regression. *Nuclear fusion*, 55(2):23012–20, 2015.
- [4] A. J. Creely, M. J. Greenwald, S. B. Ballinger, D. Brunner, J. Canik, J. Doody, T. Fülop, D. T. Garnier, R. Granetz, T. K. Gray, C. Holland, N. T. Howard, J. W. Hughes, J. H. Irby, V. A. Izzo, G. J. Kramer, A. Q. Kuang, B. LaBombard, Y. Lin, B. Lipschultz, N. C. Logan, J. D. Lore, E. S. Marmar, K. Montes, R. T. Mumgaard, C. Paz-Soldan, C. Rea, M. L. Reinke, P. Rodriguez-Fernandez, K. Särkimäki, F. Sciortino, S. D. Scott, A. Snicker, P. B. Snyder, B. N. Sorbom, R. Sweeney, R. A. Tinguely, E. A. Tolman, M. Umansky, O. Vallhagen, J. Varje, D. G. Whyte, J. C. Wright, S. J. Wukitch, and J. Zhu. Overview of the sparc tokamak. *Journal of plasma physics*, 86(5), 2020.
- [5] Blaise Faugeras. An overview of the numerical methods for tokamak plasma equilibrium computation implemented in the nice code. *Fusion engineering and design*, 160:112020–, 2020.
- [6] R. Fischer and A. Dinklage. Integrated data analysis of fusion diagnostics by means of the bayesian probability theory. *Review of Scientific Instruments*, 75(10):4237–4239, 2004.

- [7] C. Gil, G. Colledani, M. Domenes, D. Volpe, A. Berne, F. Faisse, C. Guillon, J. Morales, P. Moreau, and B. Santraine. Renewal of the interfero-polarimeter diagnostic for west. *Fusion engineering and design*, 140:81–91, 2019.
- [8] Jonathan Goodman and Jonathan Weare. Ensemble samplers with affine invariance. *Communications in Applied Mathematics and Computational Science*, 5(1):65–80, January 2010.
- [9] Ian H. Hutchinson and Ian H. Hutchinson. *Principles of plasma diagnostics / I. H. Hutchinson*. Cambridge University press, Cambridge etc, c1987.
- [10] S. Li, H. Jiang, Z. Ren, and C. Xu. Optimal tracking for a divergent-type parabolic pde system in current profile control. *Abstract and applied analysis*, 2014:1–8, 2014.
- [11] David J.C. MacKay. *Bayesian methods for adaptive models*. PhD thesis, California Institute of Technology, 1992.
- [12] P. Moreau, A. Le-Luyer, P. Spuig, P. Malard, F. Saint-Laurent, J. F. Artaud, J. Morales, B. Faugeras, H. Heumann, B. Cantone, M. Moreau, C. Brun, R. Nouailletas, E. Nardon, B. Santraine, A. Berne, P. Kumari, and S. Belsare. The new magnetic diagnostics in the west tokamak. *Review of scientific instruments*, 89(10):10J109–10J109, 2018.
- [13] Carl Edward. Rasmussen and Christopher K. I. Williams. *Gaussian processes for machine learning*. Adaptive computation and machine learning. MIT Press, Cambridge, Mass, 2006.
- [14] T. Tala, F. Eriksson, P. Mantica, A. Mariani, A. Salmi, E.R. Solano, I.S. Carvalho, A. Chomiczewska, E. Delabie, J. Ferreira, E. Fransson, L. Horvath, P. Jacquet, D. King, A. Kirjasuo, S. Leerink, E. Lerche, C. Maggi, M. Marin, M. Maslov, S. Menmuir, R.B. Morales, V. Naulin, M.F.F. Nave, H. Nordman, C. Perez Von Thun, P.A. Schneider, M. Sertoli, K. Tanaka, and Jet Contributors. Role of NBI fuelling in contributing to density peaking between the ICRH and NBI identity plasmas on JET. 62(6):066008.
- [15] G T von Nessi and M J Hole. Using bayesian analysis and gaussian processes to infer electron temperature and density profiles on the mega-ampere spherical tokamak experiment. *Review of scientific instruments*, 84(6):063505–063505, 2013.
- [16] John Wesson and John Wesson. *Tokamaks / John Wesson ; with contributions from D.J. Campbell et al.* The Oxford engineering science series. Clarendon Press, Oxford, 2. ed edition, 1997.

- [17] A. B. Zylstra, A. L. Kritcher, O. A. Hurricane, D. A. Callahan, J. E. Ralph, D. T. Casey, A. Pak, O. L. Landen, B. Bachmann, K. L. Baker, L. Berzak Hopkins, S. D. Bhandarkar, J. Biener, R. M. Bionta, N. W. Birge, T. Braun, T. M. Briggs, P. M. Celliers, H. Chen, C. Choate, D. S. Clark, L. Divol, T. Döppner, D. Fittinghoff, M. J. Edwards, M. Gatu Johnson, N. Gharibyan, S. Haan, K. D. Hahn, E. Hartouni, D. E. Hinkel, D. D. Ho, M. Hohenberger, J. P. Holder, H. Huang, N. Izumi, J. Jeet, O. Jones, S. M. Kerr, S. F. Khan, H. Geppert Kleinrath, V. Geppert Kleinrath, C. Kong, K. M. Lamb, S. Le Pape, N. C. Lemos, J. D. Lindl, B. J. MacGowan, A. J. Mackinnon, A. G. MacPhee, E. V. Marley, K. Meaney, M. Millot, A. S. Moore, K. Newman, J.-M. G. Di Nicola, A. Nikroo, R. Nora, P. K. Patel, N. G. Rice, M. S. Rubery, J. Sater, D. J. Schlossberg, S. M. Sepke, K. Sequoia, S. J. Shin, M. Stadermann, S. Stoupin, D. J. Strozzi, C. A. Thomas, R. Tommasini, C. Trosseille, E. R. Tubman, P. L. Volegov, C. R. Weber, C. Wild, D. T. Woods, S. T. Yang, and C. V. Young. Experimental achievement and signatures of ignition at the national ignition facility. *Physical review. E*, 106(2):025202–025202, 2022.

APPENDICES

Appendix A

Deriving the Closed Form Posterior Expressions

The inference begins with Bayes theorem,

$$P(\vec{y}|\vec{d}, \vec{\epsilon}, \theta) = \frac{P(\vec{d}|\vec{y}, \vec{\epsilon})P(\vec{y}|\theta)}{P(\vec{d}|\vec{\epsilon}, \theta)}, \quad (\text{A.1})$$

where the likelihood can be written as,

$$P(\vec{d}|\vec{y}, \vec{\epsilon}) = \frac{1}{(2\pi)^{\frac{m}{2}} \sqrt{|\Sigma_{li}|}} \exp \left[-\frac{1}{2} (\vec{d} - R\vec{y})^\top \Sigma_{li}^{-1} (\vec{d} - R\vec{y}) \right], \quad \Sigma_{li} = \vec{\epsilon}I, \quad (\text{A.2})$$

the prior as,

$$\begin{aligned} P(\vec{y}|\theta) &= \frac{1}{(2\pi)^{\frac{n}{2}} \sqrt{|K|}} \exp \left[-\frac{1}{2} (\vec{y} - \vec{\mu}_{pr})^\top K^{-1} (\vec{y} - \vec{\mu}_{pr}) \right], \\ \theta &\rightarrow \{\sigma, l\}, \quad K_{ij} = k(\rho_i, \rho_j) = \sigma^2 \exp \left[\frac{(\rho_i - \rho_j)^2}{2l^2} \right], \end{aligned} \quad (\text{A.3})$$

and the posterior as,

$$P(\vec{y}|\vec{d}, \vec{\epsilon}, \theta) = \frac{1}{(2\pi)^{\frac{n}{2}} \sqrt{|\Sigma_{post}|}} \exp \left[-\frac{1}{2} (\vec{y} - \mu_{post})^\top \Sigma_{post}^{-1} (\vec{y} - \mu_{post}) \right]. \quad (\text{A.4})$$

To derive $\vec{\mu}_{post}$ and Σ_{post} the likelihood and prior are multiplied together and re-arranged. Only first and second order \vec{y} terms are kept as the constants do not affect the shape of the multivariate Gaussian and thus do not affect $\vec{\mu}_{post}$ or Σ_{post} . Then using the completing the square formula for matrices they can be combined into a single multivariate Gaussian. By comparing with the posterior we find the closed form expressions for $\vec{\mu}_{post}$ and Σ_{post} . When the distributions are multiplied together the exponential powers are summed,

$$-\frac{1}{2} \left[(\vec{d} - R\vec{y})^\top \Sigma_{li}^{-1} (\vec{d} - R\vec{y}) + (\vec{y} - \vec{\mu}_{pr})^\top K^{-1} (\vec{y} - \vec{\mu}_{pr}) \right],$$

ignoring the $-\frac{1}{2}$ for now and multiplying it out gets,

$$\begin{aligned} & \left(\vec{d}^\top \Sigma_{li}^{-1} \vec{d} - \vec{d}^\top \Sigma_{li}^{-1} R \vec{y} - (R \vec{y})^\top \Sigma_{li}^{-1} \vec{d} + (R \vec{y})^\top \Sigma_{li}^{-1} R \vec{y} \right), \\ & + \left(\vec{y}^\top K^{-1} \vec{y} - \vec{y}^\top K^{-1} \vec{\mu}_{pr} - \vec{\mu}_{pr}^\top K^{-1} \vec{y} + \vec{\mu}_{pr}^\top K^{-1} \vec{\mu}_{pr} \right), \end{aligned}$$

focusing on the 1st order terms and remembering that the transpose of a scalar is itself and the transpose of a symmetric matrix (e.g. Σ_{li}) is itself, it can be shown that the first order terms equate to

$$-\vec{d}^\top \Sigma_{li}^{-1} R \vec{y} - (R \vec{y})^\top \Sigma_{li}^{-1} \vec{d} - \vec{y}^\top K^{-1} \vec{\mu}_{pr} - \vec{\mu}_{pr}^\top K^{-1} \vec{y} = -2 \vec{y}^\top (R^\top \Sigma_{li}^{-1} \vec{d} + K^{-1} \vec{\mu}_{pr}) = -2 \vec{y}^\top \vec{b}$$

in which a substitution was made to ease the use of the competing square formula,

$$\vec{b} = R^\top \Sigma_{li}^{-1} \vec{d} + K^{-1} \vec{\mu}_{pr}$$

switching the focus to the 2nd order terms,

$$(R \vec{y})^\top \Sigma_{li}^{-1} R \vec{y} + \vec{y}^\top K^{-1} \vec{y} = \vec{y}^\top (R^\top \Sigma_{li}^{-1} R + K^{-1}) \vec{y} = \vec{y}^\top M \vec{y},$$

in which a substitution was made to ease the use of the completing square formula,

$$M = (R^\top \Sigma_{li}^{-1} R + K^{-1})$$

ignoring 0 order terms that do not affect the shape, the original exponential power takes the form,

$$-\frac{1}{2} \left[\vec{y}^\top M \vec{y} - \vec{y}^\top \vec{b} \right],$$

by completing the squares we obtain

$$\vec{y}^\top M \vec{y} - \vec{y}^\top \vec{b} = (\vec{y} - M^{-1} \vec{b})^\top M (\vec{y} - M^{-1} \vec{b}) - \vec{b}^\top M^{-1} \vec{b}.$$

We can ignore $\vec{b}^\top M^{-1} \vec{b}$ as it doesn't affect the shape of the Gaussian. Finally, for the posterior we have

$$P(\vec{y} | \vec{d}, \vec{\epsilon}, \theta) \propto \exp \left[-\frac{1}{2} (\vec{y} - \vec{\mu}_{post})^\top \Sigma_{post}^{-1} (\vec{y} - \vec{\mu}_{post}) \right] \propto \exp \left[-\frac{1}{2} (\vec{y} - M^{-1} \vec{b})^\top M (\vec{y} - M^{-1} \vec{b}) \right],$$

from comparison, it can be seen that,

$$\vec{\mu}_{post} = M^{-1} \vec{b} = (R^\top \Sigma_{li}^{-1} R + K^{-1})^{-1} \left(R^\top \Sigma_{li}^{-1} \vec{d} + K^{-1} \vec{\mu}_{pr} \right), \quad \Sigma_{post} = M^{-1} = (R^\top \Sigma_{li}^{-1} R + K^{-1})^{-1}. \quad (\text{A.5})$$

The posterior mean is often written in another form. This form can be found with the following steps,

$$\begin{aligned} \vec{\mu}_{post} &= (K^{-1} + R^\top \Sigma_{li}^{-1} R)^{-1} (R^\top \Sigma_{li}^{-1} \vec{d} + K^{-1} \vec{\mu}_{pr}) \\ &= (K^{-1} + R^\top \Sigma_{li}^{-1} R)^{-1} R^\top \Sigma_{li}^{-1} \vec{d} + (K^{-1} + R^\top \Sigma_{li}^{-1} R)^{-1} (K^{-1} + R^\top \Sigma_{li}^{-1} R - R^\top \Sigma_{li}^{-1} R) \vec{\mu}_{pr} \\ &= \vec{\mu}_{pr} + (K^{-1} + R^\top \Sigma_{li}^{-1} R)^{-1} R^\top \Sigma_{li}^{-1} \vec{d} - (K^{-1} + R^\top \Sigma_{li}^{-1} R)^{-1} R^\top \Sigma_{li}^{-1} R \vec{\mu}_{pr} \\ &= \vec{\mu}_{pr} + (K^{-1} + R^\top \Sigma_{li}^{-1} R)^{-1} R^\top \Sigma_{li}^{-1} (\vec{d} - R \vec{\mu}_{pr}). \end{aligned}$$

The final closed form expression of the posterior mean and covariance is

$$\vec{\mu}_{post} = \vec{\mu}_{pr} + (K^{-1} + R^\top \Sigma_{li}^{-1} R)^{-1} R^\top \Sigma_{li}^{-1} (\vec{d} - R \vec{\mu}_{pr}) \quad (\text{A.6})$$

$$\Sigma_{post} = (R^\top \Sigma_{li}^{-1} R + K^{-1})^{-1}. \quad (\text{A.7})$$

The error of each value in $\vec{\mu}_{post}$ can be found on the diagonal of Σ_{post} .

Appendix B

Deriving the Marginal Likelihood and Loss Function Expression

The marginal likelihood is the denominator in Bayes theorem for the inference

$$P(\vec{y}|\vec{d}, \vec{\epsilon}, \theta) = \frac{P(\vec{d}|\vec{y}, \vec{\epsilon})P(\vec{y}|\theta)}{P(\vec{d}|\vec{\epsilon}, \theta)}, \quad (\text{B.1})$$

since the marginal likelihood is a normalizing constant it can be expressed as

$$P(\vec{d}|\vec{\epsilon}, \theta) = \int P(\vec{d}|\vec{y}, \vec{\epsilon})P(\vec{y}|\theta) d\vec{y}, \quad (\text{B.2})$$

the likelihood is,

$$P(\vec{d}|\vec{y}, \vec{\epsilon}) = \frac{1}{(2\pi)^{\frac{m}{2}} \sqrt{|\Sigma_{li}|}} \exp \left[-\frac{1}{2}(\vec{d} - R\vec{y})^\top \Sigma_{li}^{-1} (\vec{d} - R\vec{y}) \right], \quad \Sigma_{li} = \vec{\epsilon}I, \quad (\text{B.3})$$

and the prior is,

$$\begin{aligned} P(\vec{y}|\theta) &= \frac{1}{(2\pi)^{\frac{n}{2}} \sqrt{|K|}} \exp \left[-\frac{1}{2}(\vec{y} - \vec{\mu}_{pr})^\top K^{-1} (\vec{y} - \vec{\mu}_{pr}) \right], \\ \theta &\rightarrow \{\sigma, l\}, \quad K_{ij} = k(\rho_i, \rho_j) = \sigma^2 \exp \left[\frac{(\rho_i - \rho_j)^2}{2l^2} \right], \end{aligned} \quad (\text{B.4})$$

when multiplied together the exponential powers become

$$\begin{aligned} & \left(\vec{d}^\top \Sigma_{li}^{-1} \vec{d} - \vec{d}^\top \Sigma_{li}^{-1} R \vec{y} - (R \vec{y})^\top \Sigma_{li}^{-1} \vec{d} + (R \vec{y})^\top \Sigma_{li}^{-1} R \vec{y} \right) \\ & \quad + \left(\vec{y}^\top K^{-1} \vec{y} - \vec{y}^\top K^{-1} \vec{\mu}_{pr} - \vec{\mu}_{pr}^\top K^{-1} \vec{y} + \vec{\mu}_{pr}^\top K^{-1} \vec{\mu}_{pr} \right), \end{aligned}$$

the first order terms of \vec{y} can be simplified,

$$-\vec{d}^\top \Sigma_{li}^{-1} R \vec{y} - (R \vec{y})^\top \Sigma_{li}^{-1} \vec{d} - \vec{y}^\top K^{-1} \vec{\mu}_{pr} - \vec{\mu}_{pr}^\top K^{-1} \vec{y} = -2\vec{y}^\top (R^\top \Sigma_{li}^{-1} \vec{d} + K^{-1} \vec{\mu}_{pr}) = -2\vec{y}^\top \vec{b},$$

the second order terms of \vec{y} can be simplified,

$$(R \vec{y})^\top \Sigma_{li}^{-1} R \vec{y} + \vec{y}^\top K^{-1} \vec{y} = \vec{y}^\top (R^\top \Sigma_{li}^{-1} R + K^{-1}) \vec{y} = \vec{y}^\top M \vec{y},$$

all together, for the marginal likelihood we have

$$\begin{aligned} P(\vec{d}|\vec{\epsilon}, \theta) &= \int P(\vec{d}|\vec{y}, \vec{\epsilon}) P(\vec{y}|\theta) d\vec{y} \\ &= \frac{1}{(2\pi)^{\frac{m}{2}} \sqrt{|\Sigma_{li}|}} \frac{1}{(2\pi)^{\frac{n}{2}} \sqrt{|K|}} \exp \left[-\frac{1}{2} (\vec{d}^\top \Sigma_{li}^{-1} \vec{d} + \vec{\mu}_{pr}^\top K^{-1} \vec{\mu}_{pr}) \right] \int \exp \left[-\frac{1}{2} \vec{y}^\top M \vec{y} + \vec{y}^\top \vec{b} \right] d\vec{y}, \end{aligned} \tag{B.5}$$

performing a standard Gaussian integral we get that

$$\int \exp \left[-\frac{1}{2} \vec{y}^\top M \vec{y} + \vec{y}^\top \vec{b} \right] d\vec{y} = \frac{(2\pi)^{\frac{n}{2}}}{\sqrt{|M|}} \exp \left[\frac{1}{2} \vec{b}^\top M^{-1} \vec{b} \right],$$

all together, for the marginal likelihood we have

$$\begin{aligned} P(\vec{d}|\vec{\epsilon}, \theta) &= \int P(\vec{d}|\vec{y}, \vec{\epsilon}) P(\vec{y}|\theta) d\vec{y} \\ &= \frac{(2\pi)^{\frac{n}{2}}}{(2\pi)^{\frac{m}{2}} (2\pi)^{\frac{n}{2}} \sqrt{|\Sigma_{li}| |K| |M|}} \exp \left[-\frac{1}{2} (\vec{d}^\top \Sigma_{li}^{-1} \vec{d} + \vec{\mu}_{pr}^\top K^{-1} \vec{\mu}_{pr} - \vec{b}^\top M^{-1} \vec{b}) \right], \end{aligned}$$

where \vec{b} and M are substitutions made earlier

$$\begin{aligned}\vec{b} &= R^\top \Sigma_{li}^{-1} \vec{d} + K^{-1} \vec{\mu}_{pr} \\ M &= (R^\top \Sigma_{li}^{-1} R + K^{-1}),\end{aligned}$$

ignoring the $-\frac{1}{2}$ for now and reverting \vec{b} and M to their original form the exponential power becomes

$$\vec{\mu}_{pr}^\top K^{-1} \vec{\mu}_{pr} + \vec{d}^\top \Sigma_{li}^{-1} \vec{d} - (R^\top \Sigma_{li}^{-1} \vec{d} + K^{-1} \vec{\mu}_{pr})^\top (K^{-1} + R^\top \Sigma_{li}^{-1} R)^{-1} (R^\top \Sigma_{li}^{-1} \vec{d} + K^{-1} \vec{\mu}_{pr}),$$

the next step requires the Woodbury identity [13],

$$(A + UCV)^{-1} = A^{-1} - A^{-1}U(C^{-1} + VA^{-1}U)^{-1}VA^{-1}, \quad (\text{B.6})$$

the exponential power can thus be expanded to be

$$\vec{\mu}_{pr}^\top K^{-1} \vec{\mu}_{pr} + \vec{d}^\top \Sigma_{li}^{-1} \vec{d} - (R^\top \Sigma_{li}^{-1} \vec{d} + K^{-1} \vec{\mu}_{pr})^\top \left[K - KR^\top (\Sigma_{li} + RKR^\top)^{-1} RK \right] (R^\top \Sigma_{li}^{-1} \vec{d} + K^{-1} \vec{\mu}_{pr}),$$

this can then be rearranged to be

$$\begin{aligned}\vec{d}^\top \left\{ \Sigma_{li}^{-1} - \Sigma_{li}^{-1} R \left[K - KR^\top (\Sigma_{li} + RKR^\top)^{-1} RK \right] R^\top \Sigma_{li}^{-1} \right\} \vec{d} \\ - 2\vec{\mu}^\top K^{-1} \left[K - KR^\top (\Sigma_{li} + RKR^\top)^{-1} RK \right] R^\top \Sigma_{li}^{-1} \vec{d} \\ + \vec{\mu}^\top \left\{ K^{-1} - K^{-1} \left[K - KR^\top (\Sigma_{li} + RKR^\top)^{-1} RK \right] K^{-1} \right\} \vec{\mu},\end{aligned}$$

the second order term in \vec{d} can be reduced

$$\begin{aligned}\Sigma_{li}^{-1} - \Sigma_{li}^{-1} R \left[K - KR^\top (\Sigma_{li} + RKR^\top)^{-1} RK \right] R^\top \Sigma_{li}^{-1} \\ = \Sigma_{li}^{-1} - \Sigma_{li}^{-1} RKR^\top \Sigma_{li}^{-1} + \Sigma_{li}^{-1} RKR^\top (\Sigma_{li} + RKR^\top)^{-1} RKR^\top \Sigma_{li}^{-1} \\ = \Sigma_{li}^{-1} - \Sigma_{li}^{-1} RKR^\top \Sigma_{li}^{-1} + \Sigma_{li}^{-1} (\Sigma_{li} + RKR^\top - \Sigma_{li}) (\Sigma_{li} + RKR^\top)^{-1} RKR^\top \Sigma_{li}^{-1} \\ = \Sigma_{li}^{-1} - (\Sigma_{li} + RKR^\top)^{-1} RKR^\top \Sigma_{li}^{-1} \\ = \Sigma_{li}^{-1} - (\Sigma_{li} + RKR^\top)^{-1} (\Sigma_{li} + RKR^\top - \Sigma_{li}) \Sigma_{li}^{-1} \\ = (\Sigma_{li} + RKR^\top)^{-1},\end{aligned}$$

the first order term in \vec{d} can be reduced

$$\begin{aligned}
& -2\vec{\mu}^\top K^{-1} \left[K - KR^\top (\Sigma_{li} + RKR^\top)^{-1} RK \right] R^\top \Sigma_{li}^{-1} \\
& = -2\vec{\mu}^\top R^\top \Sigma_{li}^{-1} + 2\vec{\mu}^\top R^\top (\Sigma_{li} + RKR^\top)^{-1} RKR^\top \Sigma_{li}^{-1} \\
& = -2\vec{\mu}^\top R^\top \Sigma_{li}^{-1} + 2\vec{\mu}^\top R^\top (\Sigma_{li} + RKR^\top)^{-1} (\Sigma_{li} + RKR^\top - \Sigma_{li}) \Sigma_{li}^{-1} \\
& = -2\vec{\mu}^\top R^\top \Sigma_{li}^{-1} + 2\vec{\mu}^\top R^\top \Sigma_{li}^{-1} - 2\vec{\mu}^\top R^\top (\Sigma_{li} + RKR^\top)^{-1} \\
& = -2\vec{\mu}^\top R^\top (\Sigma_{li} + RKR^\top)^{-1},
\end{aligned}$$

the zero order term in \vec{d} can be reduced

$$K^{-1} - K^{-1} \left[K - KR^\top (\Sigma_{li} + RKR^\top)^{-1} RK \right] K^{-1} = R^\top (\Sigma_{li} + RKR^\top)^{-1} R,$$

now the exponential is

$$\begin{aligned}
& \vec{d}^\top \Sigma_{li}^{-1} \vec{d} + \vec{\mu}_{pr}^\top K^{-1} \vec{\mu}_{pr} - \vec{b}^\top M^{-1} \vec{b} \\
& = \vec{d}^\top (\Sigma_{li} + RKR^\top)^{-1} \vec{d} - 2\vec{\mu}^\top R^\top (\Sigma_{li} + RKR^\top)^{-1} + \vec{\mu}^\top R^\top (\Sigma_{li} + RKR^\top)^{-1} R \vec{\mu} \\
& = (\vec{d} - R\vec{\mu}_{pr})^\top (\Sigma_{li} + RKR^\top)^{-1} (\vec{d} - R\vec{\mu}_{pr}),
\end{aligned}$$

the scaling constant can be simplified using the matrix determinant lemma [13],

$$|A + UCV| = |A| |C| |C^{-1} + VA^{-1}U|, \quad (\text{B.7})$$

$$|\Sigma_{li}| |K| |M| = |\Sigma_{li}| |K| |R^\top \Sigma_{li}^{-1} R + K^{-1}| = |\Sigma_{li} + RKR^\top|,$$

this also helps avoid precision errors as there are fewer matrix inversions and determinants to compute. The marginal likelihood becomes

$$\begin{aligned}
P(\vec{d} | \vec{\epsilon}, \theta) &= \int P(\vec{d} | \vec{y}, \vec{\epsilon}) P(\vec{y} | \theta) d\vec{y} \\
&= \frac{1}{(2\pi)^{\frac{m}{2}} \sqrt{|\Sigma_{li} + RKR^\top|}} \exp \left[-\frac{1}{2} (\vec{d} - R\vec{\mu}_{pr})^\top (\Sigma_{li} + RKR^\top)^{-1} (\vec{d} - R\vec{\mu}_{pr}) \right].
\end{aligned} \quad (\text{B.8})$$

The values of the marginal likelihood can become very large and troublesome to compute with standard 64-bit float precision. For this reason, the logarithm is computed,

$$\ln(P(\vec{d}|\vec{\epsilon}, \theta)) = -\frac{1}{2} \left[m \ln(2\pi) + \ln(|\Sigma_{li} + RKR^\top|) + (\vec{d} - R\vec{\mu}_{pr})^\top (\Sigma_{li} + RKR^\top)^{-1} (\vec{d} - R\vec{\mu}_{pr}) \right]. \quad (\text{B.9})$$

It is convention for loss functions to be minimized so the negative log marginal likelihood is used as the loss function for optimizing the hyper-parameters. When minimizing, the constants do not play a major role, thus the loss function for the hyperparameters is expressed as

$$loss(\epsilon, \theta) = \ln(|\Sigma_{li} + RKR^\top|) + (\vec{d} - R\vec{\mu}_{pr})^\top (\Sigma_{li} + RKR^\top)^{-1} (\vec{d} - R\vec{\mu}_{pr}) \quad (\text{B.10})$$

Appendix C

Complete Set of Distributions and Expressions for Reference

C.1 Gaussian Process Regression for Interferometry, Discluding Artificial Observations

In section 2.3, Bayesian inference was introduced for a simple regression problem. In section 2.5 it was explained how to alter the method so that it could be applied to interferometry data to infer the electron density profile. Here are the mentioned distributions fully described for reference. The likelihood is,

$$\begin{aligned} \mathcal{N}(\vec{d}, \mu_{li} = R\vec{n}_e, \Sigma_{li}) &= \frac{1}{\sqrt{(2\pi)^{\frac{n}{2}} |\Sigma_{li}|}} \exp \left[-\frac{1}{2} (\vec{d} - R\vec{n}_e)^\top \Sigma_{li}^{-1} (\vec{d} - R\vec{n}_e) \right], \\ \Sigma_{li} &= \vec{\epsilon}I = \begin{bmatrix} \epsilon_1 & 0 & \cdots & 0 \\ 0 & \epsilon_2 & \cdots & 0 \\ \vdots & \vdots & \ddots & 0 \\ 0 & 0 & 0 & \epsilon_m \end{bmatrix}, \end{aligned} \tag{C.1}$$

where R is a matrix composed of flux surface contribution row vectors, where each row vector corresponds to a different line of sight and when multiplied with \vec{n}_e produces the line integrated density over that line of sight, see section 2.5 for more details. The prior is,

$$\begin{aligned}\mathcal{N}(\vec{n}_e, \vec{\mu}_{pr} = \vec{0}, K) &= \frac{1}{\sqrt{(2\pi)^{\frac{n}{2}} |K|}} \exp \left[-\frac{1}{2} \vec{n}_e^\top K^{-1} \vec{n}_e \right], \\ K_{ij} = k(\rho_i, \rho_j) &= \sigma^2 \left(\frac{2l(\rho_i)l(\rho_j)}{l(\rho_i)^2 + l(\rho_j)^2} \right)^{1/2} \exp \left(\frac{(\rho_i - \rho_j)^2}{l(\rho_i)^2 + l(\rho_j)^2} \right),\end{aligned}\tag{C.2}$$

where $l(\rho)$ can be a hyperbolic tangent function or otherwise. If l is not a function but a constant, $l(\rho) = l$, then the kernel reverts back to the stationary kernel,

$$K_{ij} = k(\rho_i, \rho_j) = \sigma^2 \exp \left[\frac{(\rho_i - \rho_j)^2}{2l^2} \right],\tag{C.3}$$

The goal is to compute the posterior,

$$\mathcal{N}(\vec{n}_e, \vec{\mu}_{post}, \Sigma_{post}) = \frac{1}{\sqrt{(2\pi)^{\frac{n}{2}} |\Sigma_{post}|}} \exp \left[-\frac{1}{2} (\vec{n}_e - \vec{\mu}_{post})^\top \Sigma_{post}^{-1} (\vec{n}_e - \vec{\mu}_{post}) \right],\tag{C.4}$$

which can be done with the closed form expressions,

$$\vec{\mu}_{post} = \vec{\mu}_{pr} + (K^{-1} + R^\top \Sigma_{li}^{-1} R)^{-1} R^\top \Sigma_{li}^{-1} (\vec{d} - R \vec{\mu}_{pr})\tag{C.5}$$

$$\Sigma_{post} = (R^\top \Sigma_{li}^{-1} R + K^{-1})^{-1},\tag{C.6}$$

as derived in appendix A. Once known the density profile can be plotted with the $\vec{\mu}_{post}$ values at the same ρ values used in the kernel. The errors are the standard deviations held in the diagonal of Σ_{post} . This calculation is unlikely to be accurate until the hyperparameters are optimised. The parameters in the length scale function $l(\rho)$ are hyperparameters. The experimental errors ϵ can also be hyperparameters if unknown. The optimal hyperparameters can be found by minimising the negative log marginal likelihood. It is derived in appendix B to be,

$$loss(\vec{\epsilon}, \theta) = \ln(|\Sigma_{li} + RKR^\top|) + (\vec{d} - R\vec{\mu}_{pr})^\top (\Sigma_{li} + RKR^\top)^{-1} (\vec{d} - R\vec{\mu}_{pr}).\tag{C.7}$$

There is no change in its form from the simple regression problem. The values of the various matrices and vectors have changed.

C.2 Gaussian Process Regression for Interferometry, Including Artificial Observations

Artificial observations can be placed in the likelihood to include prior knowledge. This circumvents precision issues when including this information in the prior. The process was explained in section 2.5. Here are the full expressions for reference. The likelihood is,

$$\begin{aligned}
\mathcal{N}(\vec{d}^{alt}, \mu_{li} = R^{alt}\vec{a}, \Sigma_{li}) &= \frac{1}{\sqrt{(2\pi)^{\frac{n}{2}} |\Sigma_{li}^{alt}|}} \exp \left[-\frac{1}{2} (\vec{d}^{alt} - R^{alt}\vec{a})^\top (\Sigma_{li}^{alt})^{-1} (\vec{d}^{alt} - R^{alt}\vec{a}) \right], \\
\vec{d}^{alt} &= \begin{bmatrix} \vec{d} \\ n_e(\rho = 1) = 0 \\ n'_e(\rho = 0) = 0 \end{bmatrix} = \begin{bmatrix} lid_1 \\ lid_2 \\ \vdots \\ lid_m \\ n_e(\rho = 1) = 0 \\ n'_e(\rho = 0) = 0 \end{bmatrix}, \\
\vec{a} &= \begin{bmatrix} \vec{n}_e \\ n_e(\rho = 1) \\ n'_e(\rho = 0) \end{bmatrix} = \begin{bmatrix} n_e(\rho_1) \\ n_e(\rho_2) \\ \vdots \\ n_e(\rho_n) \\ n_e(\rho = 1) \\ n'_e(\rho = 0) \end{bmatrix}, \\
\Sigma_{li}^{alt} &= I \begin{bmatrix} \vec{\epsilon} \\ \epsilon_{edge} \\ \epsilon'_{core} \end{bmatrix} = I \begin{bmatrix} \epsilon_1 \\ \epsilon_2 \\ \vdots \\ \epsilon_m \\ \epsilon_{edge} \\ \epsilon'_{core} \end{bmatrix} = \begin{bmatrix} \epsilon_1 & 0 & \cdots & 0 & 0 & 0 \\ 0 & \epsilon_2 & \cdots & 0 & 0 & 0 \\ \vdots & \vdots & \ddots & 0 & 0 & 0 \\ 0 & 0 & 0 & \epsilon_m & 0 & 0 \\ 0 & 0 & 0 & 0 & \epsilon_{edge} & 0 \\ 0 & 0 & 0 & 0 & 0 & \epsilon'_{core} \end{bmatrix}, \\
R^{alt} &= \begin{bmatrix} R_{m \times n} & O_{m \times 2} \\ O_{2 \times n} & I_{2 \times 2} \end{bmatrix} = \begin{bmatrix} R_{m \times n} & & 0 & 0 \\ & & \vdots & \vdots \\ & & 0 & 0 \\ 0 & \cdots & 0 & 1 & 0 \\ 0 & \cdots & 0 & 0 & 1 \end{bmatrix},
\end{aligned} \tag{C.8}$$

where \vec{d} has been altered to include the data from the artificial observations, lid_1 is the line integrated density from the 1st laser of m lasers. \vec{a} is the vector to be inferred and is the original electron density profile \vec{n}_e with the additional artificial observations, $\vec{\epsilon}$ contains the experimental errors of the interferometry for each line of sight and ϵ_{edge} is the error of our artificial observation for the electron density at the edge, it represents the strength of our prior assumption. ϵ'_{core} represents the error of the artificial observation that the density gradient is 0 at the core, it also represents the strength of this prior assumption. R is the original response matrix explained previously and R^{alt} is a small alteration to return the artificial observations when applied to some \vec{a} . The prior is,

$$\begin{aligned} \mathcal{N}(\vec{a}, \vec{\mu}_{pr} = \vec{0}, K^{alt}) &= \frac{1}{\sqrt{(2\pi)^{\frac{n}{2}} |K^{alt}|}} \exp \left[-\frac{1}{2} \vec{a}^\top (K^{alt})^{-1} \vec{a} \right], \\ K^{alt} &= \begin{bmatrix} K & K' \\ K'^\top & K'' \end{bmatrix}, \\ K_{ij} &= k(\rho_i, \rho_j) = \sigma^2 \left(\frac{2l(\rho_i)l(\rho_j)}{l(\rho_i)^2 + l(\rho_j)^2} \right)^{1/2} \exp \left(\frac{(\rho_i - \rho_j)^2}{l(\rho_i)^2 + l(\rho_j)^2} \right), \\ K'_{ij} &= k'(\rho'_i, \rho_j) = \frac{\partial k(\rho'_i, \rho_j)}{\partial \rho'_i}, \\ K''_{ij} &= k''(\rho'_i, \rho'_j) = \frac{\partial k(\rho'_i, \rho'_j)}{\partial \rho'_i \partial \rho'_j}, \end{aligned} \quad (\text{C.9})$$

where $l(\rho)$ can be a hyperbolic tangent function or otherwise. If $l(\rho) = l$ then this reverts to the stationary kernel,

$$K_{ij} = k(\rho_i, \rho_j) = \sigma^2 \exp \left[\frac{(\rho_i - \rho_j)^2}{2l^2} \right]. \quad (\text{C.10})$$

The K' and K'' are required to account for the fact that now there is gradient information and the covariance for positions of gradient information ρ' requires a differential of the original covariance kernel k . The goal is to compute the posterior,

$$\mathcal{N}(\vec{a}, \vec{\mu}_{post}, \Sigma_{post}) = \frac{1}{\sqrt{(2\pi)^{\frac{n}{2}} |\Sigma_{post}|}} \exp \left[-\frac{1}{2} (\vec{a} - \vec{\mu}_{post})^\top \Sigma_{post}^{-1} (\vec{a} - \vec{\mu}_{post}) \right], \quad (\text{C.11})$$

where since \vec{n}_e has been extended to \vec{a} the $\vec{\mu}_{post}$ and Σ_{post} have also been extended. The careful choice of alterations allows us to use the same closed form expressions as before the

artificial observations simply by inserting the alternate forms of the various matrices and vectors. The marginal likelihood for optimization also holds its form. To get the density profile one must remove the end terms of $\vec{\mu}_{post}$ associated with the artificial observations before plotting. The same applies to the diagonal of Σ_{post} to obtain the errors.

Glossary

IAT Integrated Autocorrelation Time (IAT) is a measure of how many steps it takes for a Markov chain to forget its initial state and become uncorrelated. It is defined as the sum of the normalized autocorrelations for all possible lags. It can be used to estimate the effective sample size and the Monte Carlo error of a chain. [19](#)

IMAS Integrated Modeling and Analysis Suite, is a framework and data management system. It is designed to store, manage, and analyze experimental and simulation data. IMAS provides a standardized platform for sharing and exchanging data among researchers from different institutions and countries. IMAS supports the integration of various fusion modeling codes and allows researchers to compare experimental data with simulation results. [10](#), [20](#)

MAP MAP stands for maximum a posteriori, which is a method of estimating an unknown quantity based on observed data and prior knowledge. MAP is a Bayesian approach that calculates the probability of a quantity given the data and the prior, and chooses the quantity that maximizes this probability. MAP can be used to find the most likely parameters of a probability distribution or a model that fits the data. [5](#), [17](#), [28–30](#), [36](#), [38–42](#)

MCMC Markov chain Monte Carlo (MCMC) is a technique for sampling from complex and high-dimensional probability distributions that are difficult to sample from directly. [5](#), [18](#), [19](#), [30](#), [40](#), [42](#)

MHD MHD stands for magnetohydrodynamics. It is a model of electrically conducting fluids that treats all interpenetrating particle species together as a single continuous medium. It is primarily concerned with the low-frequency, large-scale, magnetic behavior in plasmas and liquid metals. [8](#)

NICE Newton direct and Inverse Computation for Equilibrium. A code developed by Blaise Faugeras at the Centre national de la recherche scientifique (CNRS) to nu-

merically solve several plasma free-boundary equilibrium problems within a tokamak including the position of magnetic flux surfaces and the electron density profile. [5](#), [6](#), [8–10](#), [21](#), [26](#), [27](#), [30](#), [33](#), [38](#), [40–42](#)

SQP Sequential Quadratic Programming is a numerical optimization technique used to solve nonlinear constrained optimization problems. It is an iterative method that seeks to find the optimal solution to a problem by iteratively approximating it with a quadratic model and then solving this quadratic subproblem. The key idea is to successively update the solution in a way that moves closer to the optimal solution while satisfying the constraints. [10](#)

WEST Tungsten (W) Environment in Steady-state Tokamak (WEST) is a French tokamak that aims to test and validate the ITER tungsten divertor components and prepare their safe operation [4](#), [5](#), [9](#), [10](#), [20](#), [21](#), [24](#), [27](#), [29](#), [30](#), [33](#), [38](#), [40–42](#)